EXPERIMENTAL STUDY ON ROCK DEFORMATION AND PERMEABILITY VARIATION

A Thesis

by

JIHUI DING

Submitted to the Office of Graduate Studies of
Texas A&M University
in partial fulfillment of the requirements for the degree of

MASTER OF SCIENCE

Chair of Committee,	Ahmad Ghassemi
Committee Members,	Eduardo Gildin
	Stefan Hurlebaus
Head of Department,	A. Daniel Hill

August 2013

Major Subject: Petroleum Engineering

ABSTRACT

The development of a petroleum reservoir would inevitably induce a rearrangement of the in-situ stress field. The rearrangement of the stress field would then bring about a deformation of the reservoir rock and a change of the permeability. This experimental study was carried out to investigate rock deformation and its impact on axial permeability. Triaxial compression tests were conducted on Berea sandstone, Indiana limestone, Westerly granite and tuff specimens. Axial permeability was continuously measured for Berea sandstone and Indiana limestone during triaxial compression tests. The axial permeability of fractured Westerly granite specimens was also measured during hydrostatic compression tests. Acoustic emission (AE) monitoring was performed to help improve the understanding of rock deformation. Results showed that Berea sandstone and Westerly granite were relatively brittle, while Indiana limestone and tuff were relatively ductile. Rock deformation altered pore structures and the change of pore structures considerably impacted fluid flow through rock. For porous Berea sandstone and Indiana limestone, the destruction of the pore structure by rock deformation led to a decrease in axial permeability. For tight Westerly granite, fractures created by rock deformation significantly improved the ease of fluid flow. Acoustic emission response was found to be strongly dependent on rock type. Brittle Berea sandstone and Westerly granite produced high AE rates during compression tests, while ductile Indiana limestone and tuff generated very low AE rates.

DEDICATION

To my parents and my wife

ACKNOWLEDGEMENTS

I would like to thank my committee chair, Dr. Ghassemi, and my committee members, Dr. Gildin and Dr. Hurlebaus, for their guidance and support throughout the course of this research. Special thanks to Dr. Ghassemi, who gave me generous support in my graduate study.

I also want to thank Gary Stowe and Bruce R. Spears, who provided tremendous help and expertise to my experimental setup. It was my great pleasure to work with them. Special thanks to Dr. Sondergeld, who provided me with the opportunity to work in his wonderful lab.

Thanks also go to my friends and colleagues and faculty and staff of petroleum department for making my time at Texas A&M University a great experience.

Finally, thanks to my mother and father for their encouragement and to my wife for her patience and love.

NOMENCLATURE

AE	Acoustic Emission
DAQ	Data Acquisition
LVDT	Linear Variable Differential Transformer
Pc	Confining Pressure
mD	Millidarcy
nD	Nanodarcy
σ_1	Maximum Principal Stress
σ_2	Intermediate Principal Stress
σ_3	Minimum Principal Stress
τ	Shear Stress
σ	Normal Stress

TABLE OF CONTENTS

Page

Page

LIST OF FIGURES

Page

Page

Page

Page

1. INTRODUCTION

1.1 Problem statement

In petroleum engineering, the ultimate goal is to produce hydrocarbon from subsurface in a systematic and economical way. Therefore the determination of the permeability of reservoir rock is of great interest for petroleum engineers. Permeability is an important parameter that is used to quantify the quality of reservoir during exploration stage. Permeability is also a key input parameter for reservoir simulation, which has significant impact on reservoir development strategy. As oil and gas is extracted from underground, the rearrangement of in-situ stress field would inevitably induce permeability variation. However, to determine rock permeability accurately is not an easy job. Permeability not only depends on rock and fluid type, but also is a function of stress state of reservoir rock. More studies are required to obtain a better understanding of stress dependent permeability, which would be very beneficial to reservoir development.

1.2 Literature review

Experimental study has been considered as an effective way to understand rock behaviors in rock mechanics. In the early twentieth century, von Kármán (1911) conducted the classic triaxial compression test on Carrara marble. In the so-called "triaxial test", a cylindrical rock specimen was confined by a constant fluid pressure and compressed in the axial direction until rock failure occurs. It is not truly triaxial loading since the intermediate and minimum principal stresses are both equal to confining

pressure ($\sigma_2 = \sigma_3 = P_c$). However, the design of apparatus and operating procedure can be relatively easily achieved in the laboratory. After later improvement and modification, the triaxial test has become a standard rock testing technique in rock mechanics. Several years later, Böker (1915) performed a different triaxial test on Carrara marble. In his test, axial stress on cylindrical rock specimen was applied first and kept constant, and then confining pressure was increased until rock failure occurs. In this configuration, the maximum and intermediate stresses are equal to confining pressure ($\sigma_1 = \sigma_2 = P_c$).

Since then, extensive experimental studies have been carried out on different types of rocks at various loading conditions to improve our understanding on rock deformation. Handin and Hager Jr (1957) performed triaxial compression tests on 23 dry sedimentary rocks of various types, including anhydrite, dolomite, limestone, sandstone, shale and siltstone. These rocks were tested at room temperature at various confining pressures. Despite each rock type exhibits some of unique deformational behaviors, all the tested rocks show small increase in elasticity and yield stress, large increase in ultimate strength with increasing confining pressure. For some rock types like anhydrite and limestone, ductility is also enhanced by increasing confining pressure, while for other rock types like silica-cemented sandstone; they still demonstrate considerable brittle behavior at high confining pressure.

Numerous interests have been directed to the experimental study of brittle-ductile transition of rock. Paterson (1958) conducted triaxial compression tests on coarse-grained Wombeyan marble at various confining pressure up to about 100 MPa. As can

be seen in **Fig. 1.1**, uniaxial compression creates axial splitting fractures. Localized shear fracture, such as single shear fracture and conjugate shear fractures, would be developed as confining pressure increases. At very high confining pressure, deformation would fairly uniformly distribute throughout rock specimen.

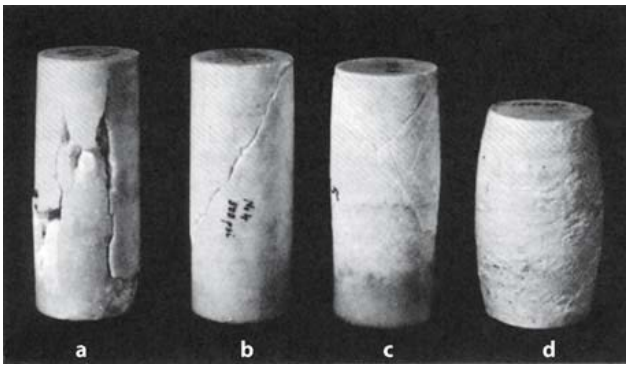

Fig. 1.1 Brittle-ductile transition of Wombeyan marble (a) Axial splitting under uniaixial compression, (b) single shear fracture under Pc = 3.5 MPa, (c) conjugate shear fracture under Pc = 35 MPa, (d) bulging under Pc = 100 MPa (Paterson, 1958)

Since fluid is often present in rock formations, numerous efforts have been made on the study of the effect of fluid pressure on rock deformation. The most commonly referred effective stress law is developed by Terzaghi (1923) which states that the effective stress responsible for the mechanical behavior of rock is equal to the total stress subtracted by fluid pressure. A number of rock properties are dependent on the effective stress, including permeability, fracture strength, elastic modulus and wave velocity etc. Brace and Martin (1968) conducted triaxial experiments on two types of crystalline rocks of low porosity at various confining pressures, pore pressures and strain rates.

Comparison of fracture strengths at different experimental configurations allowed them to test the validity of the effective stress law. They found that a critical loading rate exists which is a function of rock type, fluid type and geometrical factors. Below this critical loading rate, the law of effective stress holds true even for low porosity rocks.

Rock deformation would inevitably impact rock properties. One of these properties that have attracted great interest is the transport property of rock formation, as it is an important aspect of rock mining such petroleum exploration. The key parameter for transport property of rock is permeability, which is observed to depend on stress subjected on rock. Numerous experimental studies have been conducted to investigate the effect of stress state on rock permeability. Brace et al. (1968) developed an experimental setup for measuring permeability of Westerly granite using pulse decay method. Water and argon were used as fluid medium. Various combinations of confining and pore pressures were selected to yield an effective confining pressure up to 400 MPa. It was found that Darcy's law still holds for fluid flow in nanodarcy scale. The permeability of Westerly granite varied markedly under different effective confining pressure, ranging from 350 nD at 10 MPa effective confining pressure to about 4 nD at 400 MPa pressure. The strong dependence of permeability on effective confining pressure implies that high pore pressure would make rock relatively more permeable.

Brace (1978) compiled fluid permeability data of different rock types from literature and showed pronounced variation in stress dependent permeability for different rock types. For low porosity rock such as Westerly granite, permeability first decreases slightly with increasing stress in confined compression test, then it increases

dramatically as the sample is approaching failure. An increase of several-fold was observed at around 80 percent of the fracture stress. For high porosity rock such as Darley Dale sandstone, the permeability variation with increasing stress is similar to granite, except that permeability prior to failure increases only 20 percent and for some cases even drops a few percent. For granular aggregates, however, permeability decreases dramatically with increasing confining pressure. It was found by Zoback and Byerlee (1975); Zoback and Byerlee (1976) that the law of effective stress breaks down for sand and sandstone based on the observations of hydrostatic and triaxial compression tests. Experimental results also show that permeability of rocks containing joints or fractures is highly sensitive to changes of effective stress.

Walsh (1981) theoretically analyzed the effect of confining and pore pressures on fracture permeability. The fluid flow rate through fracture can be viewed as the product of two factors: one describes the effect of aperture and the other one describes the effect of tortuosity. The effect of aperture on flow rate is much more pronounced than that of tortuosity. The effect of pore pressure and confining pressure on fluid flow through fractures can be described by effective stress law $P_e = P_c - \partial P_p$. The coefficient ∂ is not always equal to one as indicated in many literatures. It was found that ∂ depends on the topography of fracture surfaces and rock type. If the fracture is created by tensile failure, ∂ is very close to unity. But for polished smooth fracture surfaces, ∂ could be as low as 0.56. If a joint is filled with clay, ∂ is more likely to be greater than unity.

Wang and Park (2002) performed triaxial compression tests on sedimentary rocks and permeability was measured for a complete stress-strain process. Experimental

results show that rock permeability changes with rock deformation. Permeability decreases at initial loading and starts to increase as specimen is approaching failure. At strain softening stage in the stress-strain curve, permeability reaches its peak value. After that permeability drops a little but still maintain at a level higher than initial value. It is obvious that permeability is significantly enhanced after rock failure.

Another frequently used experimental technique in rock mechanics is acoustic emission (AE) monitoring. During rock deformation, some processes such as microcracking, pore collapse and frictional sliding can generate acoustic waves. Detection and analysis of AE signal provide useful information to help us better understand deformational behavior of rock. Lockner (1993) reviewed the successes and limitations of acoustic emission monitoring in the study of rock fracture. He divided the laboratory studies of AE test into four categories 1) the study of damage development in rock during loading through the counting of AE events; 2) the study of fracture nucleation and growth through the determination of AE source locations; 3) the study of source mechanism through the analysis of AE full waveform data; 4) the study of rock properties through detecting AE wave velocities and attenuation.

The most commonly used AE technique is the counting of AE events. Scholz (1968) developed an AE testing system of high sensitivity. With this system, he tested several types of rocks at confining pressure up to 500 MPa to investigate the microcracking processes during rock deformation. A typical stress-strain curve with AE activity is shown in **Fig. 1.2**. For brittle rocks, such as Westerly granite, the inelastic deformation was found to be directly proportional to AE activity. It was concluded that

the phenomenon of dilatancy in brittle rocks can be completely accounted for by the microcracking processes. For ductile rocks and frictional sliding, AE activity behaved quite differently from that of brittle rocks. Since Griffith's criterion is not applicable to rock, a simple statistical model based on the inhomogeous nature of rock was introduced to describe the microcracking processes during rock deformation.

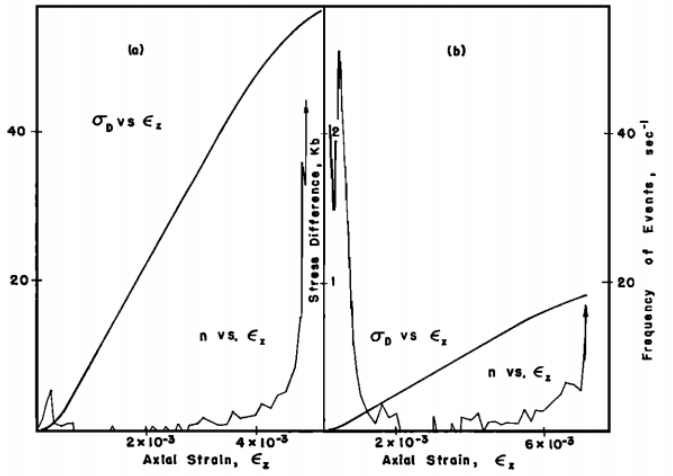

Fig. 1.2 Stress & AE activity versus strain for two rocks in uniaxial compression (a) Westerly granite; (b) Colorado rhyolite tuff (Scholz, 1968)

Lockner and Byerlee (1977) conducted creep tests on Weber sandstone and Westerly granite samples with AE monitoring. Two samples for each type were tested by stepping differential stresses up to rock strength at constant confining pressure of 100 MPa. At each stress level, the acoustic emission rate ν was found to decay exponentially with the total number of events N. Mathematically it takes the form $\log\nu = \beta - \alpha N$, where α and β are constants. Experimental results also show that α decreases

systematically with increasing differential stress and becomes negative as sample approaches failure. Among many empirical creep laws, Lomnitz's relation was found to best fit the experimental data.

The Kaiser effect is a well-known phenomenon of acoustic emission in metallurgy. It was found that a material under loading would emit acoustic waves only after the previous load level is exceeded. Kaiser (1950) first observed this phenomenon in tensile tests of metals. In rock mechanics, the Kaiser effect has been used to determine in-situ stress through testing oriented cores from underground with AE monitoring. Holcomb (1993) interpreted the Kaiser effect based on a micromechanical model developed by Costin (1983). Using the concept of damage surface, it was shown that the prediction from the theory agrees well with experimental observation. The micromechanical model also helps explain why the commonly-used uniaxial loading method (ULM) for determining in-situ stress is not valid. An alternative method, the extensional loading method (ELM), was developed to determine general stress histories.

Hirata (1987) conducted uniaxial compression test on basalt with AE monitoring. The sample was loaded to about 85% of its fracture strength. Then the axial stress was held constant until fracturing occurs. Individual bursts of AE events were identified from the creep stage and treated as mainshock-aftershock sequences. Two models, the Omori's power law model and the exponential decay model, were used to describe the time series characteristics of the shock sequences. It was found that the AE bursts changed from exponential decay to power law decay as the sample approaches failure. Analysis of p-value in the Omori's law for different AE burst sequences shows it

decreases with stress. It is believed that the decrease of p-value during the evolution of the fracture process may serve as precursor of earthquake and the estimation of the degree of fracture of the local crust.

To study fluid pressure diffusion in rock, Kranz et al. (1990) conducted fluid injection tests with AE monitoring. Three experiments with different loading configurations were presented. AE Source locations and focal mechanisms were determined for each experiment. Results showed that it is very difficult to monitor fluid migration by simply analyzing AE signals induced solely by fluid pressure diffusion. The reason is that only with sufficient differential stress can diffusing fluid produce useful AE signals, both the differential stress and fluid diffusion (deceases effective confining pressure) can result in damage in rock and it is very difficult to distinguish between the two AE generation mechanisms. A model was also established to explain the difficulty.

In order to investigate the role of pre-existing cracks in rock fracture, Lei et al. (2000) performed triaxial tests on two types of crystalline rock. With most other properties being the same, the only difference between the two rocks is that one contains main large pre-existing cracks, whereas the other one is almost crack-free. Experimental results showed significant different responses in AE activities under triaxial compression. The sample with large pre-existing cracks showed low AE activity and increasing b-value before fault nucleation. On the contrary, the crack-free sample showed strong AE activity and short-term b-value anomalies. These results confirmed that the faulting process, especially the nucleation, is predominantly governed by pre-existing cracks.

The dominant role of pre-existing crack can be explained by the fact that stress concentration at a crack tip is generally much severer than that caused by other types of heterogeneity.

Stanchits et al. (2006) measured compressional (P), shear (S) wave velocities, AE activity of basalt and granite samples in both triaxial and hydrostatic compression tests. While hydrostatic pressure was increased to 120 MPa, P-wave velocity increased more than 50% and 20% for basalt and granite, respectively. AE source mechanism analysis showed that pore collapse was dominant during compaction. In triaxial loading, evolution of velocity field demonstrated that anisotropy in basalt was more pronounced than in granite. In the early loading stage, tensile failure was the dominant source mechanism. As the sample approached failure, more double couple (shear) events were identified, which revealed that shear cracks interconnected previously formed tensile cracks and eventually leaded to faulting.

Fortin et al. (2009) applied AE technique in the test of porous sandstone samples. Three experiments are reported which exhibits three different modes of deformation, namely shear localization, compaction localization and cataclastic compaction. It was shown that critical stress states at which pore collapse and grain crushing occur are well corresponded to a surge in both cumulative AE events and AE rate. Spatial and temporal distribution of AE source location revealed that preexisting cracks and high porosity regions control the nucleation process in the early stage of loading. As loading progresses, AE events tend to uniformly distribute across the sample in hydrostatic loading (cataclastic compaction), while in triaxial loading AE events nucleate either

around the faulting plane (shear localization) or several compaction bands (compaction localization). Source locations are in good agreement with microstructural observation of the samples using SEM. Source mechanism analysis demonstrated that pore collapse and shear type events dominate in all three experiments and only a small number of tensile type events are identified.

1.3 Objectives of this study

This study will be mainly based on experimental investigation and the objectives of this study include the following.

1. Prepare experimental setup and measure permeability of different rock types under various stress states.
2. Analyze the effect of rock type and stress state on permeability.
3. Characterize the acoustic response during rock deformation.

2. EXPERIMENTAL SETUP

2.1 General description of experimental setup

The experimental setup for this study consists of three sub-systems: triaxial rock testing system, permeability measurement system and acoustic emission monitoring system. All the equipment is shown **Fig. 2.1**. Detailed description of each sub-system will be given in the following sections.

Fig. 2.1 Photo of the experimental setup

2.2 Triaxial rock testing system

2.2.1 General description

The triaxial rock testing system used in this work was manufactured by Geotechnical Consulting & Testing Systems (GCTS). The major components of the

triaxial rock testing system include load frame, high pressure triaxial cell, hydraulic pump, confining and pore pressure cabinets, data acquisition cabinet and software. The schematic diagram of GCTS triaxial rock testing system is shown in **Fig. 2.2**.

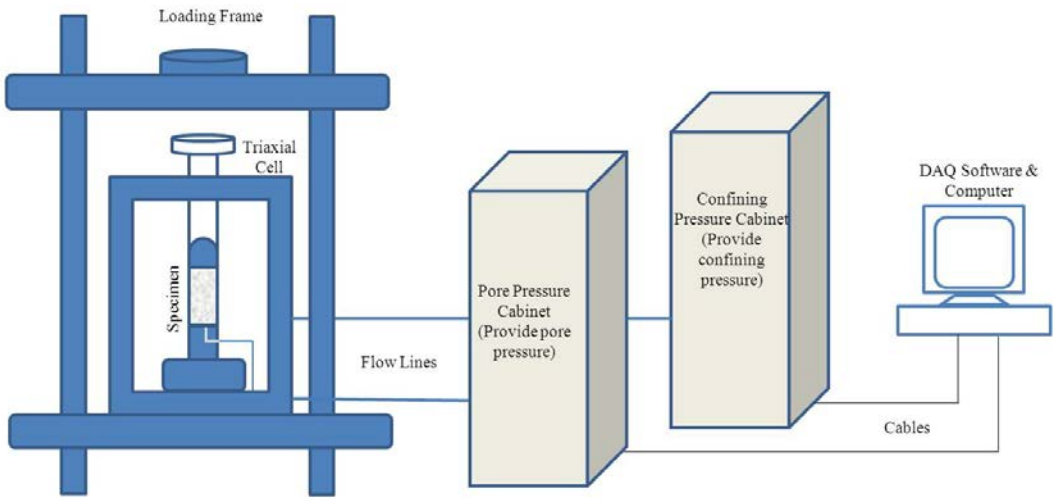

Fig. 2.2 Schematic diagram of GCTS triaxial rock testing system

The loading system has 1,500 kN load capacity and 1,750 kN/mm stiffness. The high pressure cell (Model HTRX-200) can accommodate rock specimens with a diameter ranging from 25 mm to 100 mm and with the ratio of height to diameter of 2. The cell is capable of applying up to 210 MPa confining pressure and 3,500 kN axial load. Forty-eight high pressure electrical feedthroughs allow connections for LVDT transducer, acoustic emission sensor and other gauges. Both confining pressure and pore pressure cabinets are installed with HPVC-210 pressure intensifier which can generate up to 210 MPa fluid pressure. The load cell, confining and pore pressure transducers

were well calibrated by the manufacturer and calibration files were stored in the data acquisition software.

During triaxial compression test, the axial and radial displacements of rock specimen are measured by LVDT transducers, which were not calibrated by the manufacturer. Therefore, calibration of LVDT transducers was performed at the very beginning of triaxial test. The LVDT transducer calibrator, which has a precision of 0.0025 mm, is shown in **Fig. 2.3**. With this calibrator, two axial and one circumferential LVDTs were calibrated between -2.5 and +2.5 mm using ten points in the DAQ software.

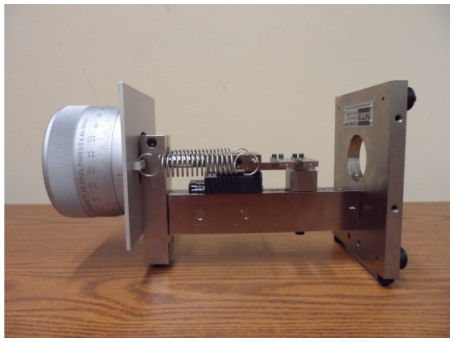

Fig. 2.3 LVDT transducer calibrator

2.2.2 Data acquisition

The data acquisition and control of triaxial test are achieved by SCON-2000 digital controller and CATS 1.8 software, both of which are produced by GCTS. The SCON-2000 digital controller applies direct closed-loop digital servo control of axial stress, axial strain, radial strain, confining and pore pressures, and several other

variables. The CATS 1.8 is a Graphical User Interface (GUI) software that allows easy and rapid control and record of triaxial test. **Fig. 2.4** shows typical software screen layout for triaxial test.

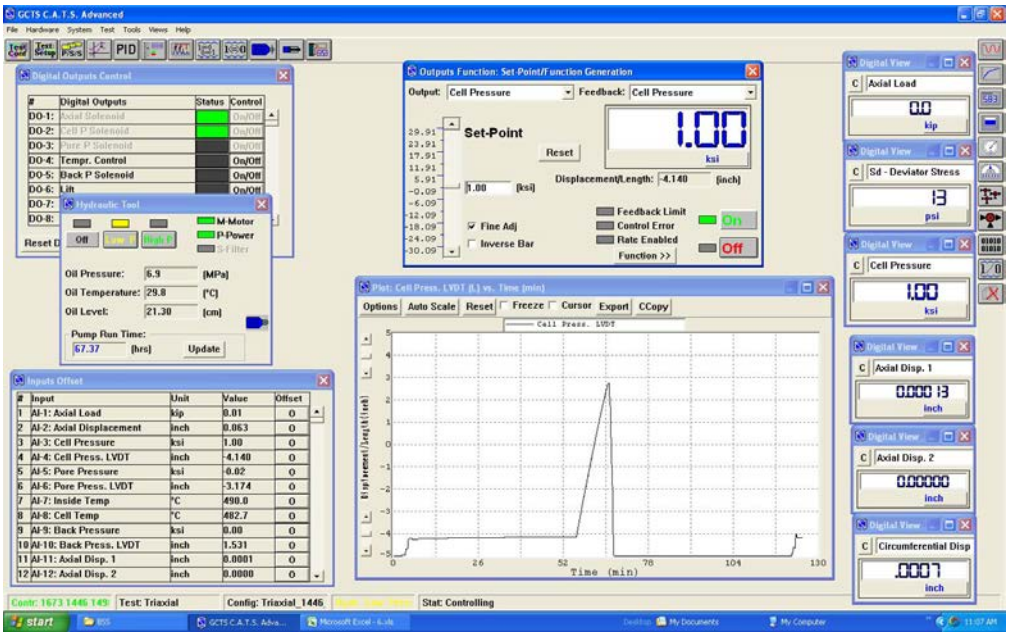

Fig. 2.4 DAQ Software screen layout of triaxial rock testing system (GCTS)

2.3 Permeability measurement system

2.3.1 General description

The permeability measurement system is incorporated in triaxial rock testing system, as is shown in **Fig. 2.5**.

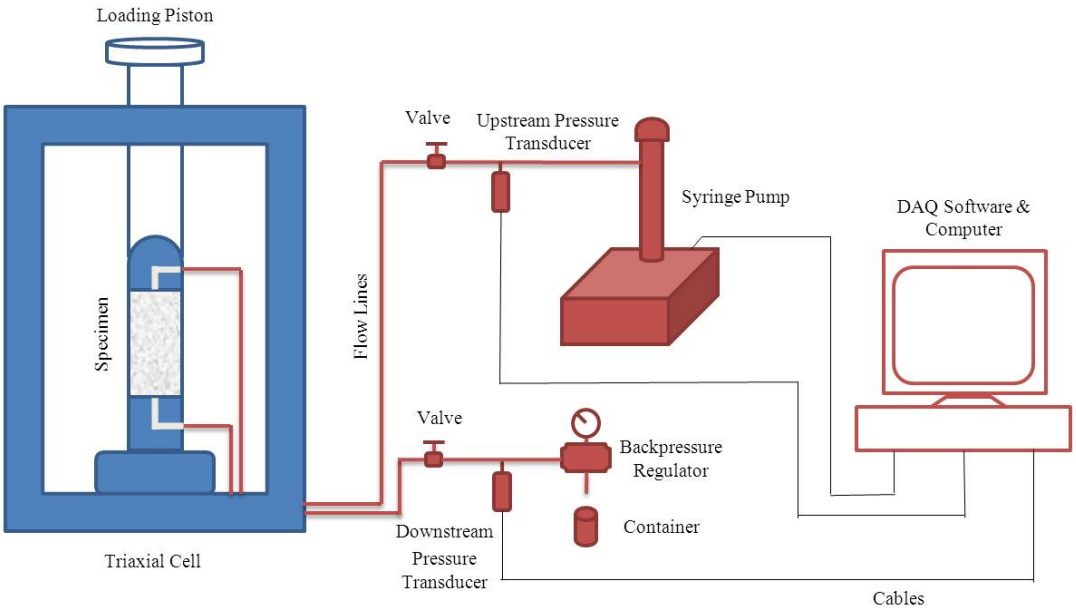

Fig. 2.5 Schematic diagram of permeability measurement system

The permeability measurement system was built based on steady state method, which requires the measurements of fluid flow rate, upstream and downstream pressures. TeledyeIsco D-series pump was used to provide accurate and continuous flow. Two HEISE DXD series digital pressure transducers were used for pressure measurement. These pressure transducers have an accuracy of $\pm 0.02\%$ of full scale, including the effects of nonlinearity, hysteresis, non-repeatability and temperature. In order to obtain more accurate measurement of differential pressure across rock specimen, the downstream pressure was elevated to around 2.1 MPa. In the triaxial cell, flow lines were connected to top and bottom loading platens, which has been carved with multiple flow channels (**Fig. 2.6**) and allow uniform fluid diffusion across end surfaces of rock specimen.

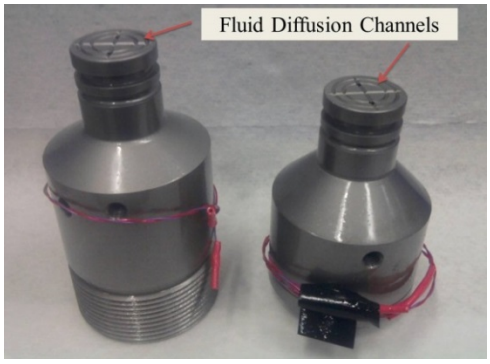

Fig. 2.6 Loading platens with carved fluid diffusion channels

2.3.2 Data acquisition

Microsoft Visual BASIC program was created to record flow rate and pressure readings from syringe pump and pressure transducers, respectively. The start time of permeability measurement was also recorded and used to correlate permeability with triaxial compression test. The screen layout of the DAQ program is shown in **Fig. 2.7**.

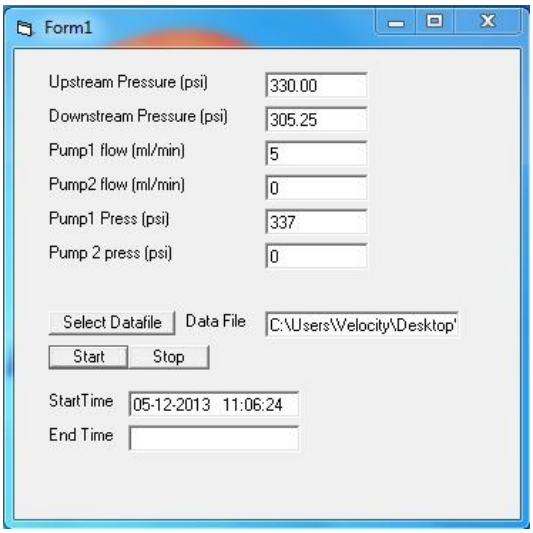

Fig. 2.7 DAQ program screen layout of permeability measurement

2.4 Acoustic emission monitoring system

2.4.1 General description

In order to monitor acoustic emission response of rock specimen during triaxial test, P-wave AE sensor was coupled inside loading platen. Besides, the AE system also includes preamplifier, filter, amplifier and signal conditioning board. The schematic diagram of acoustic emission monitoring system is shown in **Fig. 2.8**.

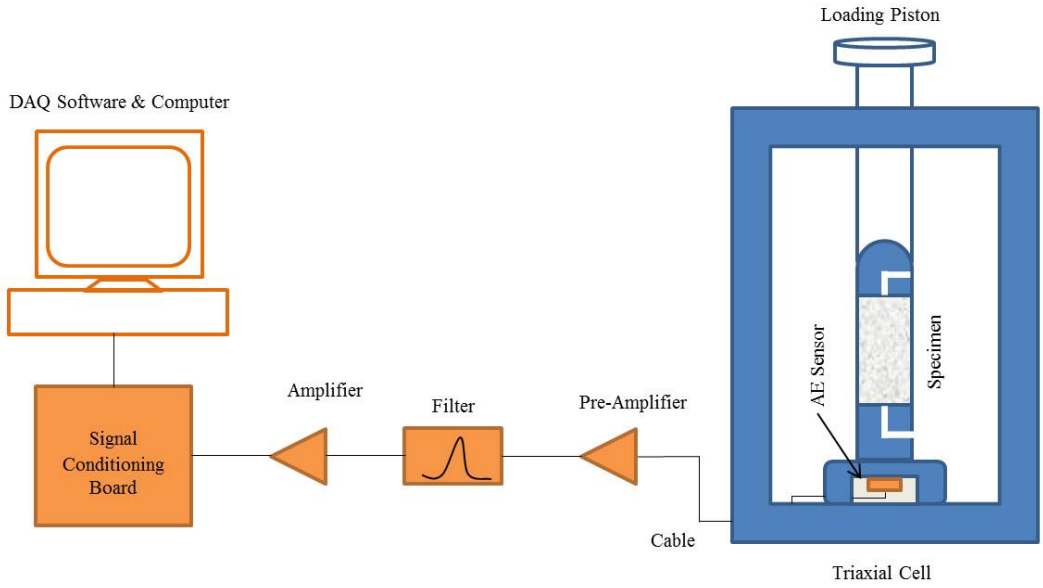

Fig. 2.8 Schematic diagram of acoustic emission monitoring system

AE signal generated during rock deformation propagates through loading platen and is detected by AE sensor bonded with the platen. AE sensor converts acoustic vibration into electric voltage. Since AE signal is usually very weak and always accompanied by lasting background noise, preamplifier is used to amplify small

electrical signals for further processing, as well as to reduce the effects of noise and interference. Then the signal is filtered by band-pass frequency filter to eliminate low and high frequency noise. After further amplification and conditioning, AE signal is displayed and analyzed with the aid of DAQ software.

2.4.2 Data acquisition

The data acquisition of AE signal is achieved using a single channel AE digital signal processor (USB AE Node) and AEwin software, both of which were produced by Physical Acoustics Corporation. USB AE Node can be easily interfaced to a computer and allows rapid acquisition of time-based AE features, such as count, event and waveform. AEwin DAQ software is capable of real-time AE feature and waveform processing, as well as 2-D & 3-D graphing. **Fig. 2.9** shows typical screen layout of AE DAQ software.

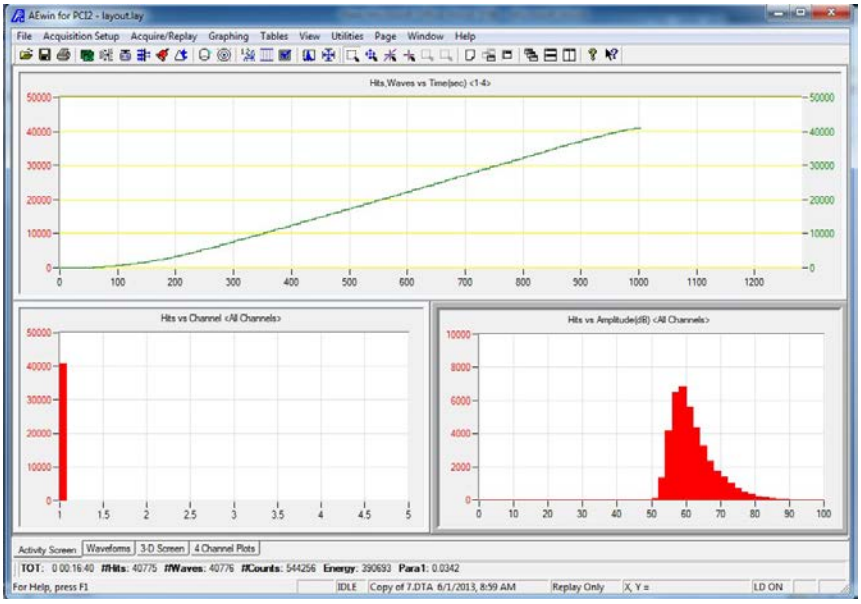

Fig. 2.9 DAQ Software screen layout of AE monitoring

3. EXPERIMENTAL PROCEDURE

3.1 Specimen preparation

Rock specimens were first cored from rock block in one-inch diameter. Then they were cut into approximately two inch in length with an electrical saw. End surfaces of rock specimens were then polished in Buehler polishing machine. Rock specimens were further polished in Brown and Sharp 818 micromaster hydraulic surface grinder to obtain a parallelness of end surfaces within 0.025 mm. All the specimens of the same rock type were cored from the same rock block, therefore uniformity in properties were maintained.

3.2 Triaxial compression test

3.2.1 Installation of loading platens and LVDT transducers

The first step of triaxial compression test is to install loading platens and LVDT transducers on specimen. The procedure is as follows.

1. Measure and record the diameter and length of rock specimen to be tested.
2. Slide rock specimen into heat-shrinkable jacket and install top and bottom loading platens, heat the jacket with a heat gun until jacket wrap around rock specimen tightly.
3. Tighten jacket with both top and bottom platens by applying two-round wires. This will make an initial sealing between rock specimen and confining fluid.
4. Install two axial LVDT ring holders and make sure they are horizontal and on the specimen.

5. Install two axial LVDTs and one circumferential LVDT and fix them in place.
6. Measure and record axial gauge length which is the distance between the centers of top and bottom LVDT ring holders. This parameter will be used to calculate axial strain.

Fig. 3.1 Photo of rock specimen installed with loading platens and LVDT transducers

After finishing the above procedure, the rock specimen is ready to be installed into triaxial cell. **Fig. 3.1** shows an example of a well prepared rock specimen installed with platens and transducers.

The next step is to install rock specimen into triaxial cell by screwing bottom platen into triaxial cell base. The rock specimen should be handled with care and make sure every part is still tight when screwing bottom platen. Then connect gauge cables with feedthroughs in the triaxial cell base and hook up flow lines to top and bottom

platens. Before closing triaxial cell, all three LVDTs should be adjusted and make sure they are in the appropriate range. The total measuring range of LVDTs is between -2.5 and +2.5 mm. For axial LVDTs, it is usually placed around -1.3 mm before test, which gives enough stroke when rock is compressed. For circumferential LVDT, it is usually set up to be around zero since rock specimen can either shrink in hydrostatic compression test or expand in triaxial compression test.

After appropriate configuration of LVDT transducers, triaxial cell is closed and placed under loading actuator. Then triaxial cell is filled with confining oil through confining pressure cabinet. At this stage, it is import to check readings of LVDTs from DAQ software and make sure they are still in the pre-configurated position. If not, triaxial cell should be opened and LVDT transducers should be set up again until they work properly. Otherwise, it makes no sense to run a test as strain measurement is not accurate.

3.2.3 System leak check

As triaxial cell is full of confining oil, it is necessary to check if there is any leaking throughout the system. The method to check is to apply a small confining pressure and watch the cell pressure intensifier LVDT versus time curve. The system is well sealed if the curve first increases and then stays constant once the target confining pressure is reached. If the curve keeps increasing and the desired confining pressure cannot be achieved, it is an indication of leaking. If this happens, stop applying confining pressure and drain confining oil out of triaxial cell, check all the fitting connections and rock specimen setup to identify the location of leak.

3.2.3 Preloading of rock specimen

If the system passes leak check, it is now ready to preload rock specimen before running a test. In preloading, a small differential stress is first applied on rock specimen as seating stress, which allows rock specimen and loading platens to be in good contact. Then confining pressure is slowly increased to the target value. At this stage, it is also important to keep an eye on cell pressure intensifier LVDT versus time curve and make sure good seal is maintained throughout the test. Confining pressure and seating stress are held until the readings from LVDT transducers stop changing, which indicates both the rock specimen and system is stable and ready for testing. Before starting a test, make sure to zero LVDT transducers through DAQ software.

3.3 Permeability measurement

In this work, axial permeability was measured continuously during triaxial test. The measurement of axial permeability includes system leak check, air elimination and rock specimen saturation.

3.3.1 System leak check

Before conducting permeability measurement, the flow lines are checked for leak section by section. First, upstream valve is closed, and then syringe pump is set up with a constant pressure. If the target pressure can be reached in a short time and flow rate varies between -0.001 and +0.001 ml/min, this section passes leak check. If not, change fitting and tubing and redo leak check until a good seal along flow line is guaranteed. After checking upstream section, open upstream valve and connect upstream and downstream lines without installing rock specimen, close downstream valve and start

pumping at constant pressure. The criterion for leak test is same as before. After checking downstream flow lines, open downstream valve and set up pressure constraint in the backpressure regulator, and start pumping at constant flow rate. If the downstream pressure can be kept at the desired pressure, the system is free of leaking. By performing leak check in this way, it is easy to identify the location of leaking and change fitting or tubing accordingly.

3.3.2 Air elimination

During the preparation of rock specimen, air is often trapped in the flow lines due to pump fill and connection/disconnection of fittings. Air is much more compressible than water and hence brings about errors in the measurement of pressure and flow rate. It is necessary to eliminate air from the system before every test. To get rid of air from pump, pump is always filled up at slow flow rate. Then immerse discharge line into water and start pumping. If no bubble was observed from discharge line for about three minutes, the pump is free of air and can be connected to permeability measurement system. During the saturation of rock specimen in the triaxial cell, the discharge line is also immersed into water. Usually it is expected to see bubbles come out of water intermittently at the beginning of saturation. The saturation process is always kept long enough to make sure all the air has been removed from the system.

3.3.3 Rock specimen saturation

Before starting triaxial test, rock specimens are fully saturated. The saturation process is long enough so that not only air is removed from the system, but also a constant initial differential pressure across rock specimen is obtained.

3.4 Acoustic emission monitoring

3.4.1 Threshold amplitude determination

Acoustic emission test is always accompanied by lasting background noise. Sources of acoustic noise include fluid flow in pumps and valves, vibration of structures and any friction processes etc. In our lab, the hydraulic pump for triaxial machine is a major source of noise. One way to deal with noise is to set up threshold amplitude for AE wave signal in the DAQ software. Only the signal with higher amplitude than the threshold can be recorded by the DAQ software. This is an effective way to eliminate the lasting low amplitude noise. However, the threshold value should be determined with caution. High threshold value is helpful in filtering noise, but it would also reject true signal as well, which negatively affects the integrity of real data. Therefore, before loading rock specimen, the AE testing system would keep running until steady response is achieved, as is shown in **Fig. 3.2**. Then the threshold amplitude is determined accordingly. Take Fig. 3.2 as an example, the main background noise is below 55dB. As a result, the threshold amplitude should be set as 55 dB during test. This process should be performed before each test, since environmental noise may vary with time.

3.4.2 Pencil lead break test

Once threshold amplitude is set up in the DAQ software, it is also advisable to perform pencil lead break test to check AE system. As the name implies, the lead of a mechanical pencil is broken around AE sensor, which is a perfect imitation of rock fracturing process. Then AE response is checked through software. By doing this, the sensitivity of AE system is verified. **Fig. 3.3** presents typical AE response during pencil

lead break test. Pencil lead was broken five times which were all well responded in the AE monitoring system. This indicates the system is ready for real test.

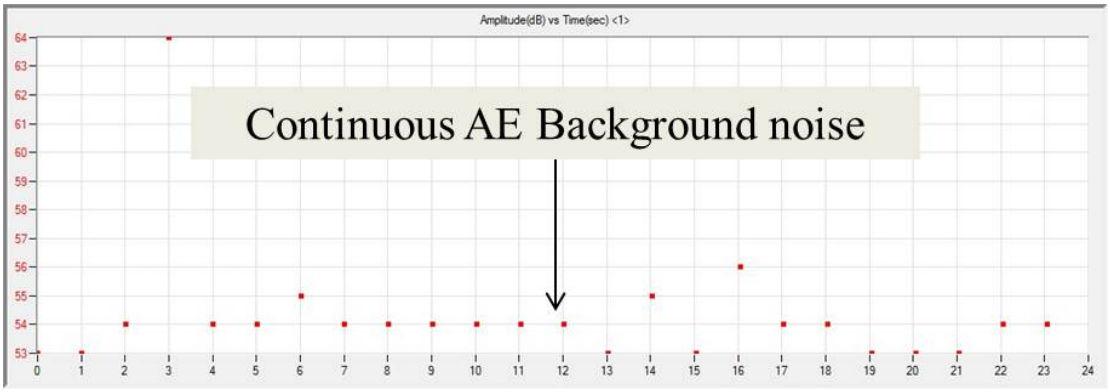

Fig. 3.2 Detection of AE background noise

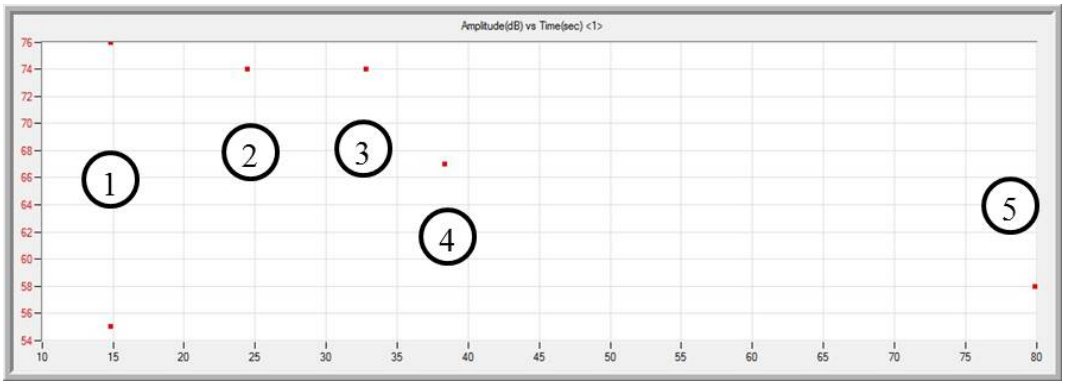

Fig. 3.3 Pencil lead break test (five times)

4. RESULTS & DISCUSSION

4.1 Sample description

In this study, four different types of rocks are selected for testing, including Berea sandstone, Indiana limestone, Westerly granite and tuff. It is intended to test different rock type with various permeability levels. For each rock type (except tuff), specimens used in the test are cored from the same block so that uniform properties can be maintained between specimens. **Fig. 4.1** shows photos of specimens of different rock type used in the test. A brief description of these rocks will be given in the following paragraphs.

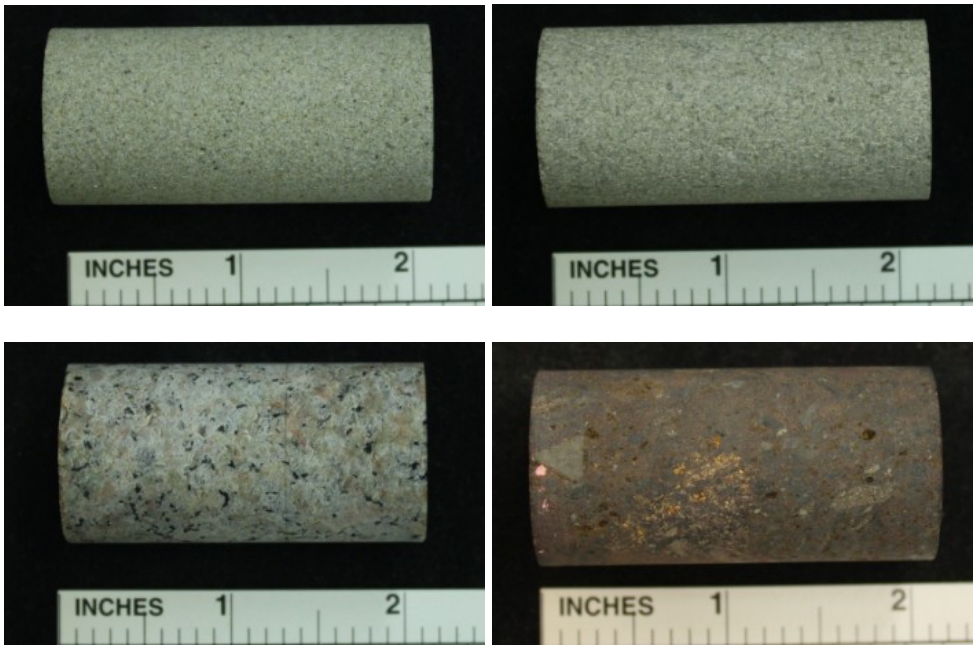

Fig. 4.1 Photos of rock specimens (from top left to bottom right: Berea sandstone, Indiana limestone, Westerly granite and tuff)

Berea sandstone has been widely used in the laboratory for mechanical and petrophysical experiments. It is a sedimentary rock which is predominantly composed of quartz. Berea sandstone has relatively high porosity and permeability which makes it a good reservoir rock. The AP-608 Automated Permeameter-Porosimeter was used to measure gas permeability and porosity of several Berea sandstone specimens. The average gas permeability and porosity are 364 mD and 20.1%, respectively, at confining pressure of 5.7 MPa.

Indiana limestone has also been widely tested in the laboratory. It is also a type of sedimentary rock which is predominantly composed of calcium carbonate. Comparing to Berea sandstone, Indiana limestone has lower porosity and permeability. The measured gas permeability and porosity are 3.36 mD and 12.67%, respectively, at confining pressure of 5.7 MPa.

Westerly granite is a type of igneous rock which is granular in texture. It has low permeability which is in nanodarcy scale. Brace et al. (1968) reported the permeability of Westerly granite of 350 nD at 10 MPa confining pressure.

Tuff is a type of rock that is composed of consolidated volcanic ash or dust ejected during volcanic eruption. It is our interest to study this type of rock. However, unlike the other three rocks, we have very limited tuff specimens. In this study, three tuff specimens were tested, which were labeled as Tuff-3V, Tuff-4V and Tuff-1H. Visual inspection shows certain heterogeneity between these specimens.

4.2 Triaxial compression test

Triaxial compression tests were performed on all four types of rock to study their deformational behaviors. Except for tuff, various confining pressures were used in triaxial compression tests. For tuff, since only three specimens were available to us, we decided to test them in the formation pressure.

4.2.1 Berea sandstone

Triaxial compression tests were performed at four different confining pressure levels. **Fig. 4.2** shows the stress-strain curves of four triaxial compression tests, while **Fig. 4.3** shows combined differential stress-axial stress curves. At relatively low confining pressures (8.2 MPa, 18.5 MPa), Berea sandstone exhibits brittle fracturing, which is marked by a drastic stress drop at the time of failure. A single shear-induced fracture can be observed on specimen after test. As confining pressure increases to higher levels (32.2 MPa, 45.9 MPa), Berea sandstone becomes ductile, without showing drastic decrease in differential stress at the time of failure. According to Wong et al. (1997), Berea sandstone is experiencing a transition from brittle faulting to cataclastic flow.

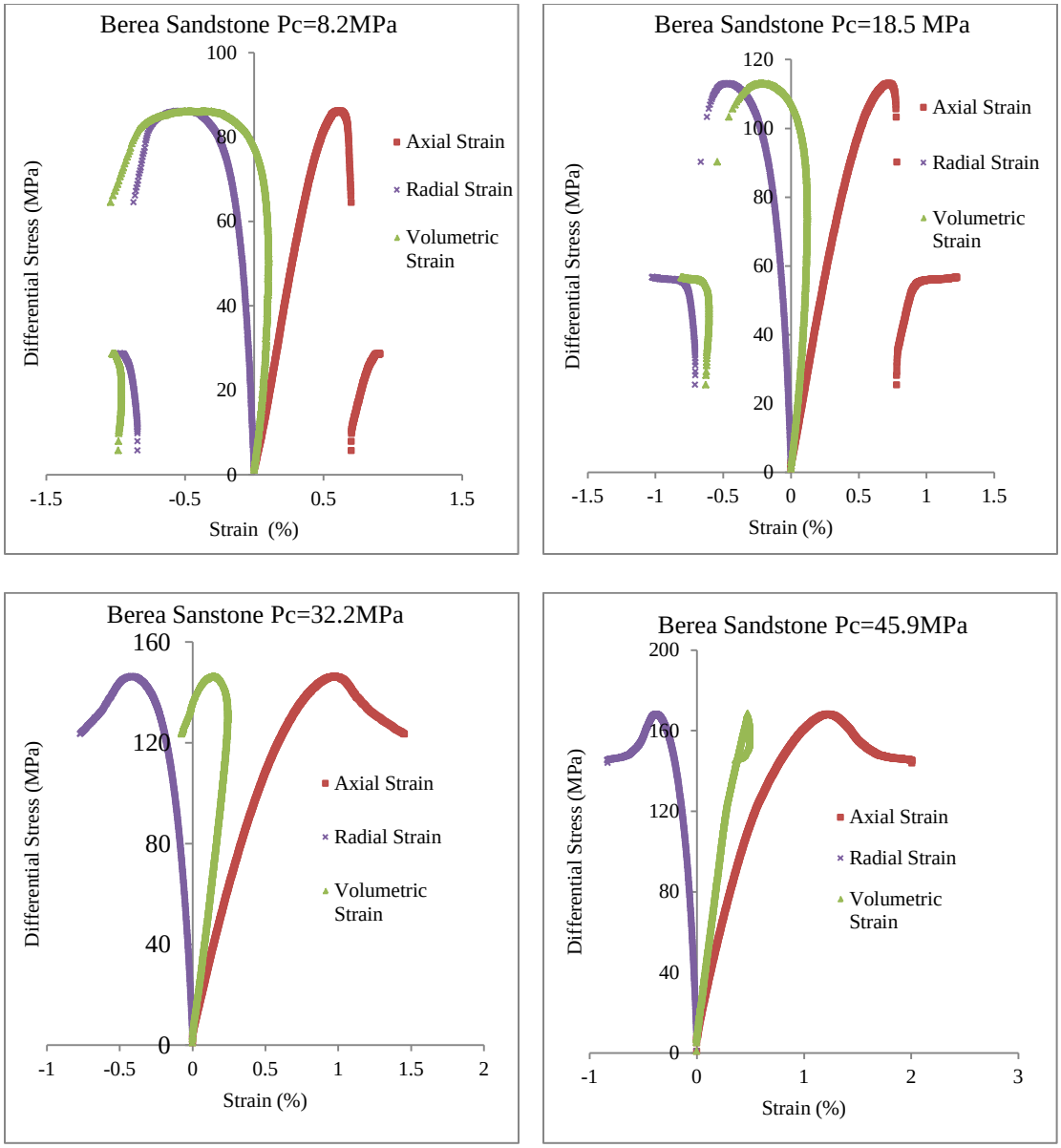

Fig. 4.2 Stress-strain curves at different confining pressures (Berea sandstone)

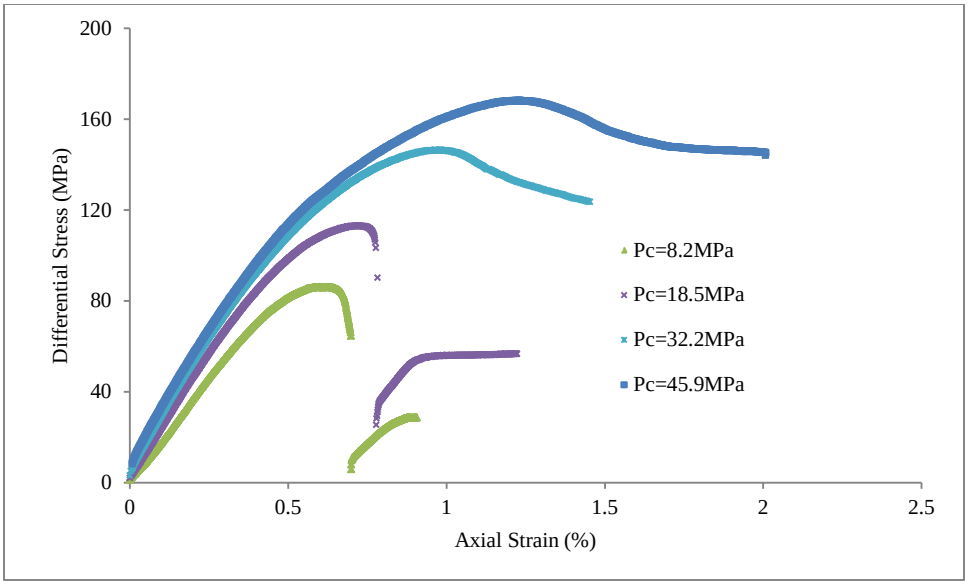

Fig. 4.3 Combined differential stress-axial strain curves at different confining pressures (Berea sandstone)

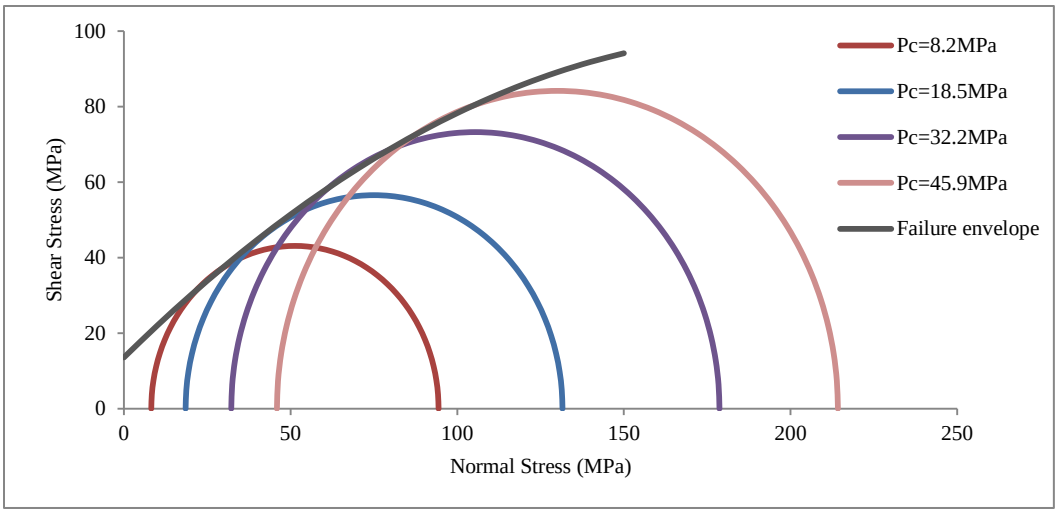

Fig. 4.4 Mohr circles and failure envelop (Berea sandstone)

Failure envelope was established based on triaxial test data (peak stress) and is shown in **Fig. 4.4**. Clearly, the failure envelope cannot be fit by Mohr-Coulomb failure criterion, which states a linear relationship between shear stress and normal stress.

Instead, the failure envelop is better fit by curved line, which has the following expression.

$$\tau = -0.0022\sigma^2 + 0.867\sigma + 13.567$$

Where τ is shear stress in MPa, σ is normal stress in MPa.

Fig. 4.5 shows a photo of rock specimens after test. At lower confining pressures (8.2 MPa, 18.5 MPa), one though-going fracture extended to about two thirds of the length of each rock specimen. At higher confining pressures (32.2 MPa, 45.9 MPa), two short fractures developed at one end of each rock specimen.

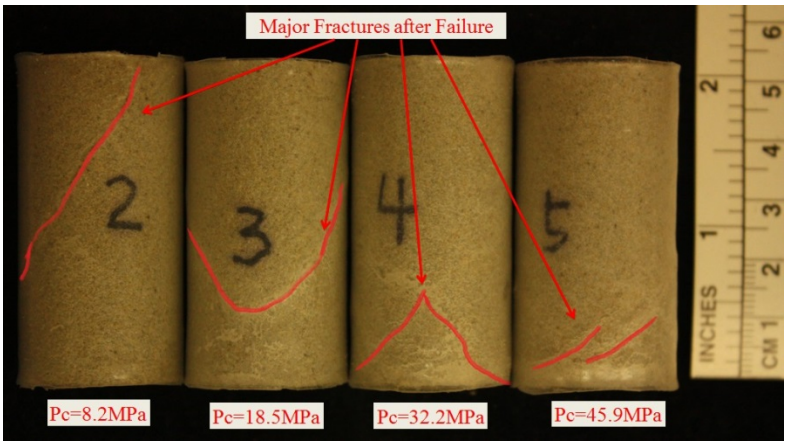

Fig. 4.5 Rock specimens after test (Berea sandstone)

4.2.2 Indiana limestone

Triaxial compression tests were performed at three different confining pressure levels. **Fig. 4.6** shows the stress-strain curves of three triaxial compression tests, while **Fig. 4.7** shows combined differential stress-axial stress curves. It can be clearly seen

that Indiana limestone displays markedly ductile feature at all three confining pressures. Differential stress drops only several megapascals after peak strength even at low confining pressure level (10.9 MPa). Comparing to Berea sandstone, Indiana limestone is much more ductile in nature.

Failure envelope was also established for Indiana limestone based on triaxial test data (peak stress), which is shown in **Fig. 4.8**. For Indiana limestone, the failure envelope is best fit by linear relationship, which has following expression.

$$\tau = 0.514\sigma + 17.067$$

Where τ is shear stress in MPa, σ is normal stress in MPa.

Fig. 4.9 shows a photo of Indiana limestone specimens after test. In three tests, only the specimen tested at lower confining pressures (10.9 MPa) developed evident fracture. The other two specimens have no noticeable fractures. This is also a strong evidence for ductile behavior.

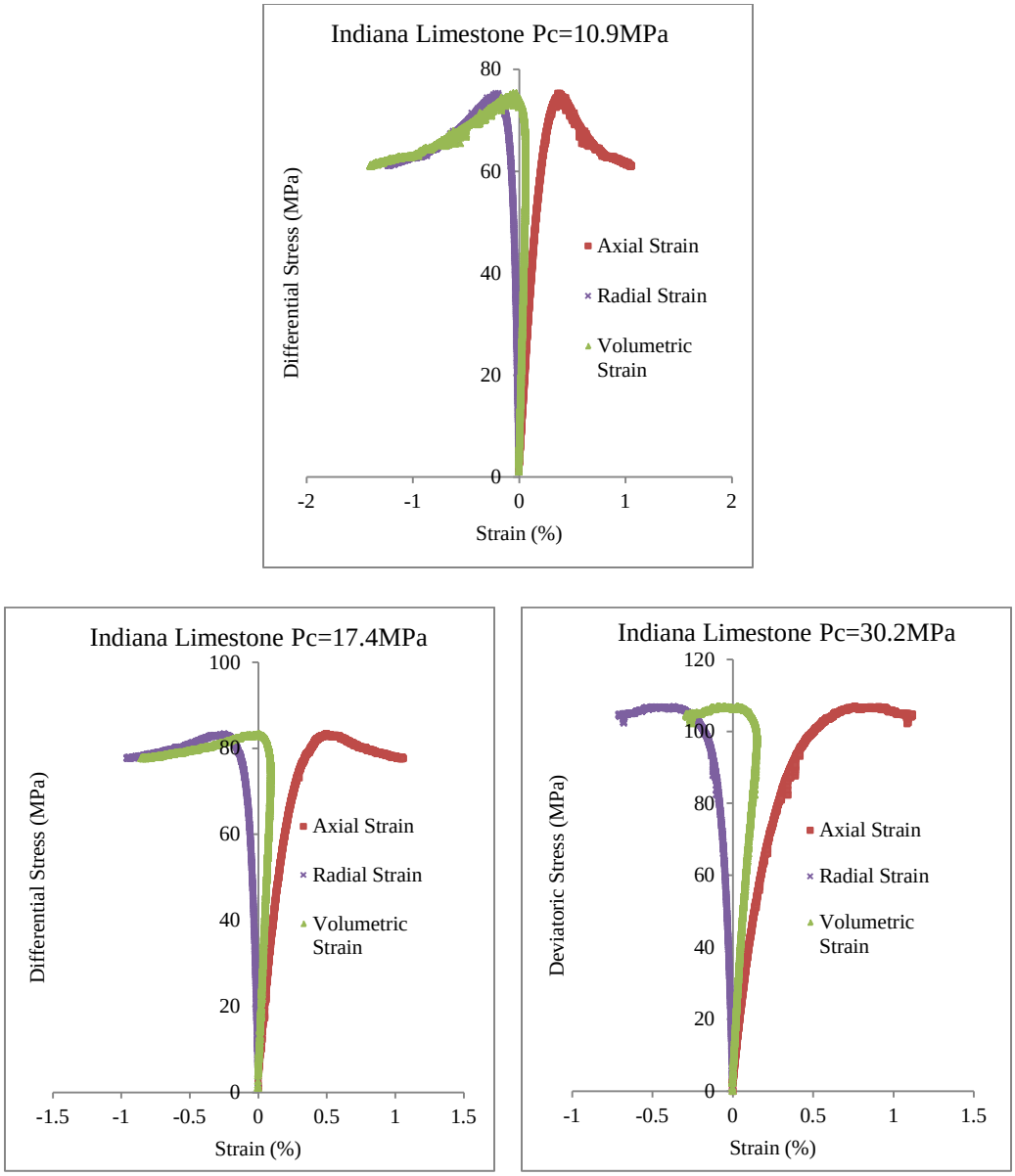

Fig. 4.6 Stress-strain curves at different confining pressures (Indiana limestone)

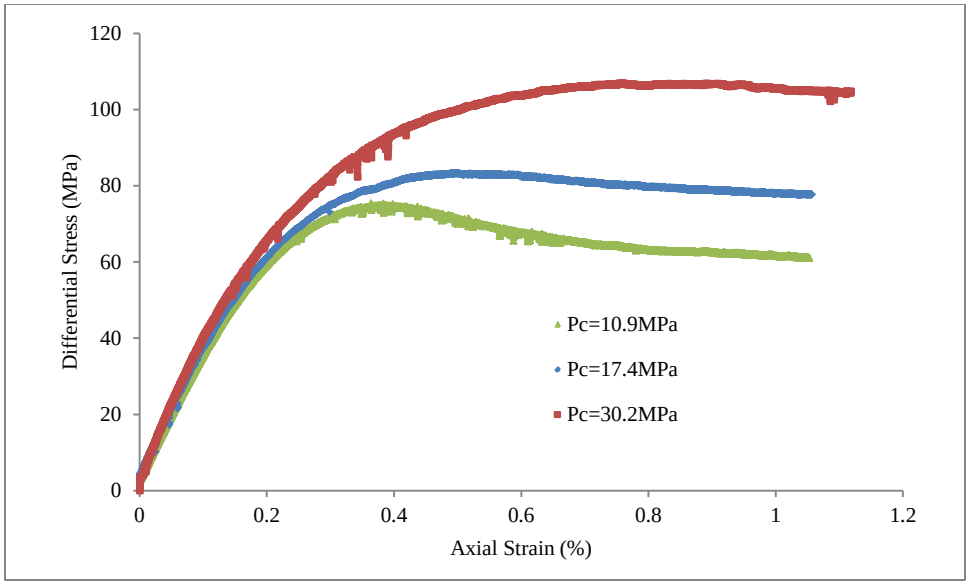

Fig. 4.7 Combined differential stress-axial strain curves at different confining pressures (Indiana limestone)

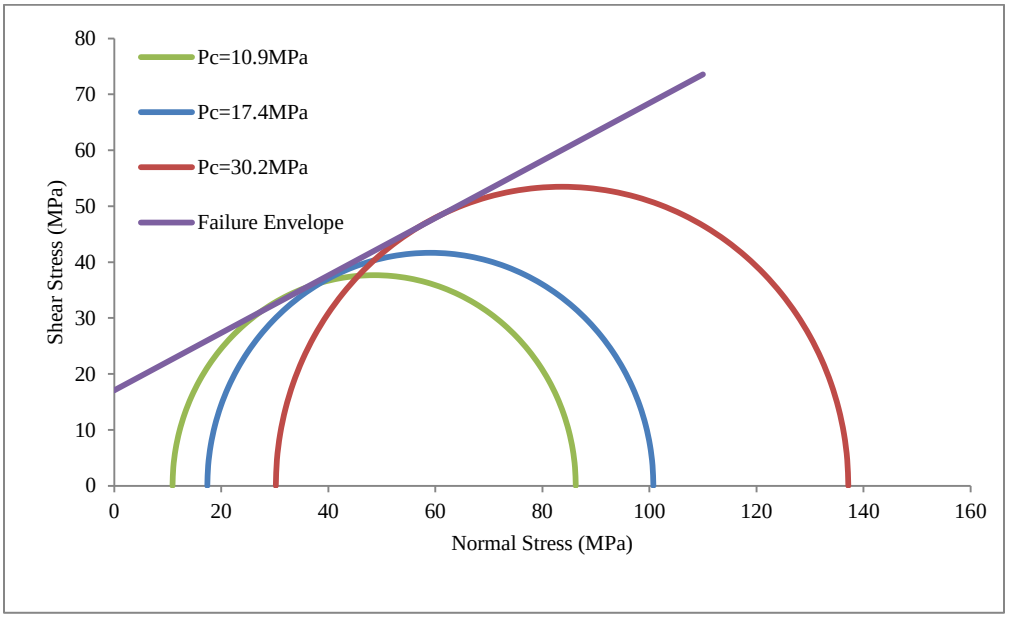

Fig. 4.8 Mohr circles and failure envelop (Indiana limestone)

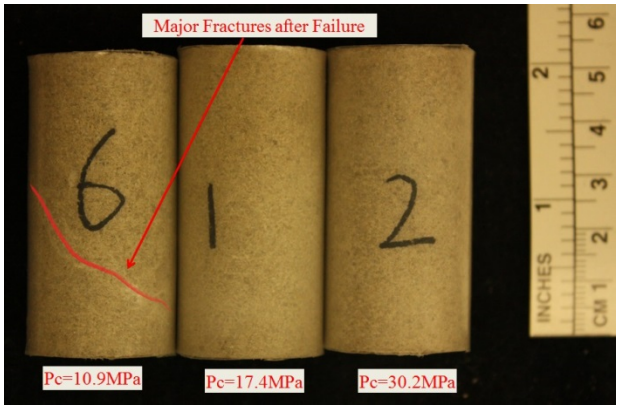

Fig. 4.9 Rock specimens after test (Indiana limestone)

4.2.3 Westerly granite

One uniaxial compression and two triaxial compression tests were conducted on Westerly granite. **Fig. 4.10** presents the stress-strain curves, while **Fig. 4.11** shows combined differential stress-axial stress curves. It can be seen that Westerly granite is very brittle. For uniaxial compression test, axial stress dropped to almost zero instantly at the time of failure, during which the DAQ system didn't catch any data. For two triaxial compression tests, Westerly granite was failed by brittle fracturing, characterized by a drastic stress decrease after peak stress.

Fig. 4.12 shows a photo of Westerly granite specimens after test. For uniaxial compression, multiple vertical fractures are observable on rock specimen. For other two tests, at least one through-going fracture was created. All three specimens look much darker after test than before test. This is because permeability measurement was attempted after failure and confining oil leaked into specimen at the end of permeability measurement.

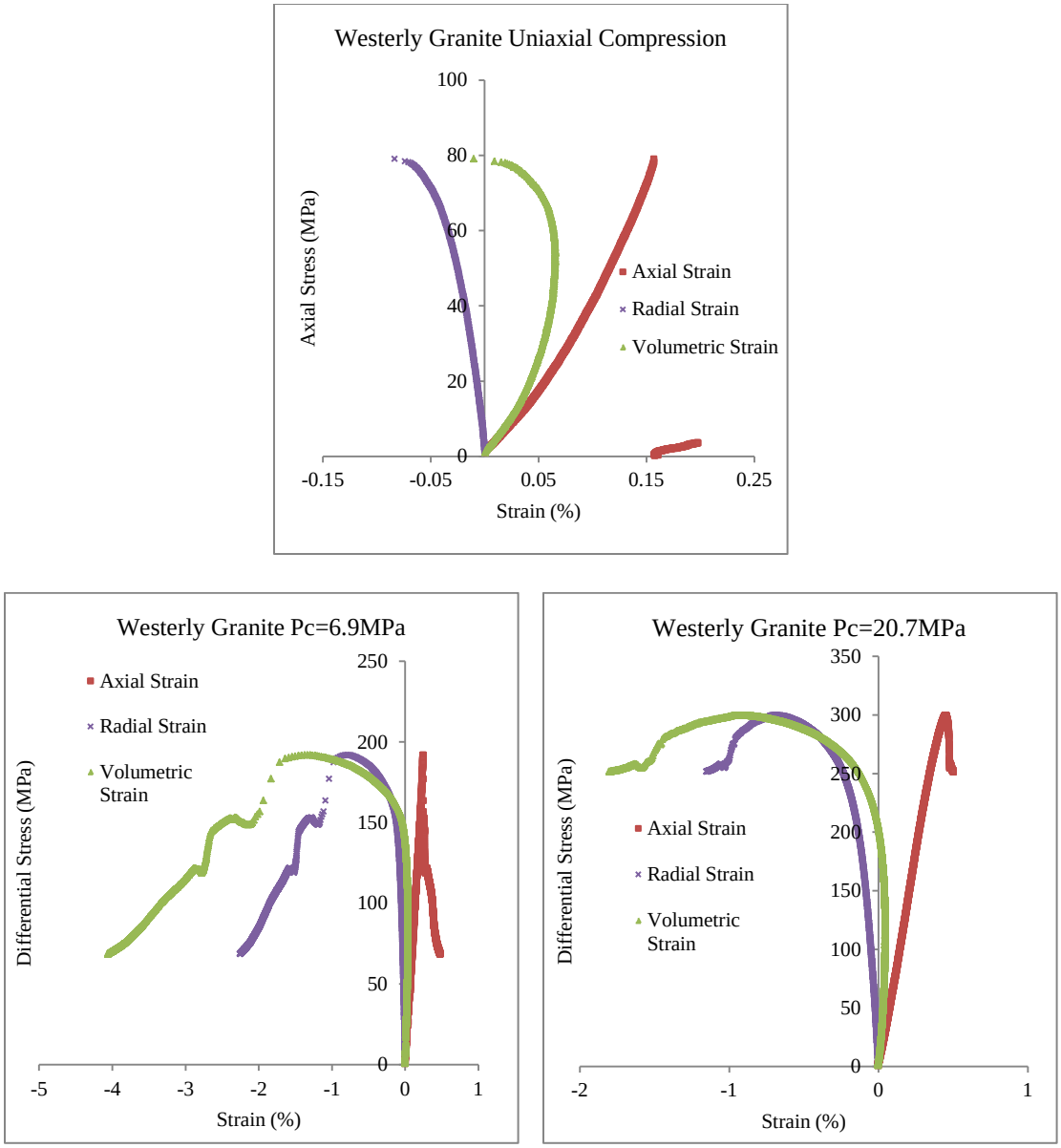

Fig. 4.10 Stress-strain curves at different confining pressures (Westerly granite)

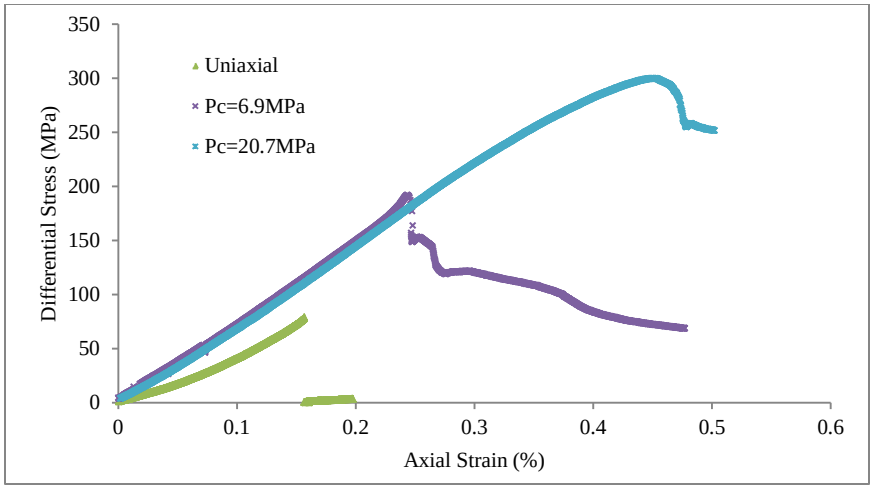

Fig. 4.11 Combined differential stress-axial strain curves at different confining pressures (Westerly granite)

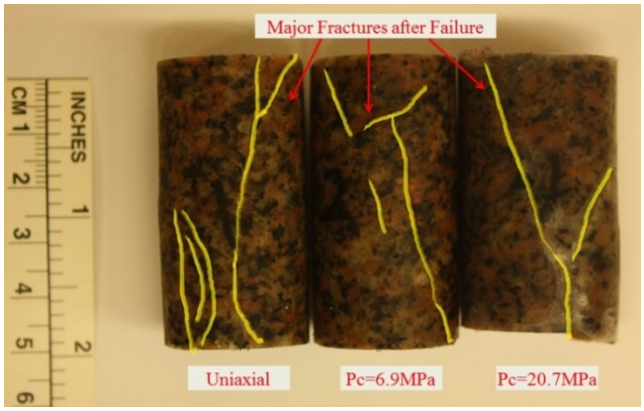

Fig. 4.12 Rock specimens after test (Westerly granite)

4.2.4 Tuff

Since we have only three tuff specimens, we decided to test these specimens at formation pressure, which is about 20.7 MPa. **Fig. 4.13** shows triaxial compression data for three tuff specimens, while **Fig. 4.14** shows combined differential stress-axial stress curves. Even tested at the same confining pressure, the stress strain curves of three

specimens exhibit considerable difference. This is most likely due to the heterogeneity between specimens. At this confining pressure, tuff-3V and tuff-4V exhibit appreciably ductile deformation.

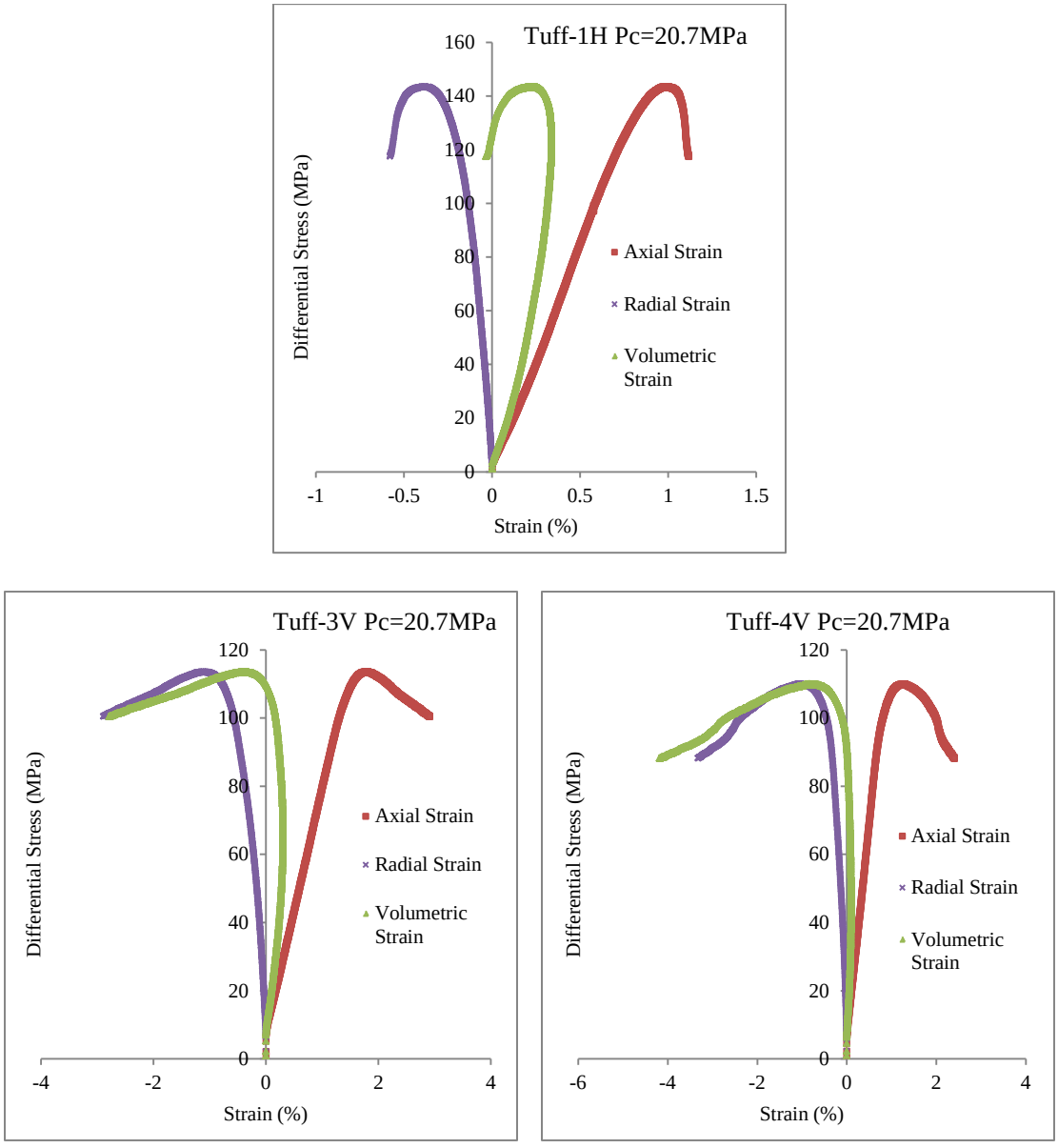

Fig. 4.13 Stress-strain curves at same confining pressures (tuff)

Fig. 4.15 shows a photo of tuff specimens after test. For all of these tests, one through-going fracture was created in each of these specimens. Axial permeability measurement was attempted after failure. But none of them was successful. The reason is that the intact rock is really tight and fluid cannot flow through. The generated macroscopic fracture didn't connect end surfaces, where pore fluid was injected into. Thus it was also impossible to flow fluid in the axial direction. For tuff-4V, confining oil leaked into specimen as plastic jacket was broken during deformation of rock specimen.

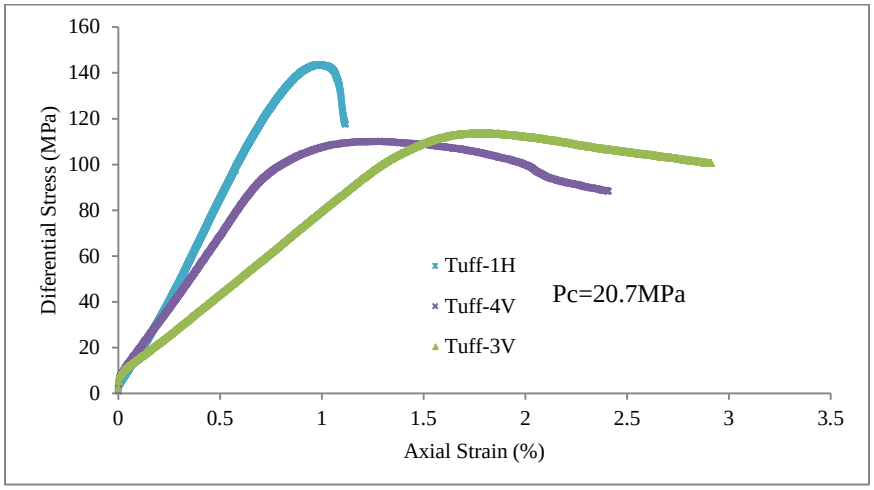

Fig. 4.14 Combined differential stress-axial strain curves at same confining pressures (tuff)

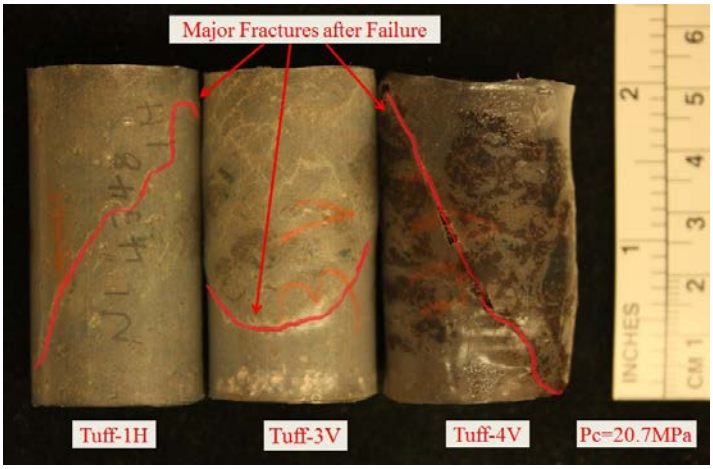

Fig. 4.15 Rock specimens after test (tuff)

4.2.5 Summary

In this section, the triaxial compression test data of four types of rocks was analyzed. It can be seen that Berea sandstone and Westerly granite demonstrate significant brittle behavior, while Indiana limestone exhibits strong ductile behavior. Tuff specimens were tested at the same confining pressure and show appreciable heterogeneity.

4.3 Permeability measurement

In order to study the dependence of permeability on stress, axial permeability measurement was carried out during triaxial compression test. Berea sandstone and Indiana limestone are permeable enough to allow continuous permeability measurement throughout compression test. For Westerly granite and tuff, the permeability of their intact samples is in nanodarcy scale. Our current experimental setup is not capable of measuring such a low permeability. Instead, we attempted to measure axial permeability

of fractured rock specimen. However, not all of those measurements on tight rock turned out to be successful. One reason is the leak of confining oil due to rock specimen breakage. Before failure specimen jacket was already deformed with the deformation of rock specimen. Further loading can easily break jacket, which is problematic for permeability measurement of fractured rock. Another reason is that the through-going fracture developed at high confining pressure test does not connect all the way to top and bottom platens through which fluid is injected into rock specimen. Fluid still cannot flow through rock specimen in the axial direction even with fracture present. As a result, we were only able to measure axial permeability of fractured Westerly granite. None of the axial permeability measurement on tuff specimens was successful.

During axial permeability measurement, differential pressure across rock specimen was measured while flowing deionized water under constant flow rate. With measured differential pressure and specimen dimension, axial permeability can be calculated based on Darcy's law. In this study, it is intended to measure axial permeability continuously during the process of rock deformation. Therefore, it is necessary to verify that the permeability measurement system can respond quickly enough to give the instantaneous axial permeability as stress on rock specimen varies. A verification test was performed, which increases differential stress at a constant rate and then holds the differential stress for some time. The obtained axial permeability is compared with stress to check if they are well correlated to each other. In a typical triaxial compression test, rock specimen is usually compressed under constant strain rate. In the verification test, the constant strain rate control is not favorable because constant

stress cannot be accomplished by maintaining a constant strain. Analysis of triaxial compression data shows that the majority part of the constant strain rate controlled test has a stress rate lower than 0.35 MPa/second. Take the triaxial compression test on Berea sandstone as an example (**Fig. 4.16)**, the stress rate exceeds 0.35 MPa/second at the beginning test. This is because the triaxial machine tries to adjust itself to achieve the target strain rate. After the system is stabilized, stress rate goes below 0.35 MPa/second. At the time of failure, especially brittle fracturing, the stress rate can be much higher than 0.35 MPa/second. As it is impractical to use a very high stress rate in the verification test due to the limitation of testing system, the measured axial permeability at the time of failure may not be the instantaneous axial permeability. But it is believed that the trend of axial permeability change can still be observed as the rate of stress change goes back to below 0.35 MPa/second after failure.

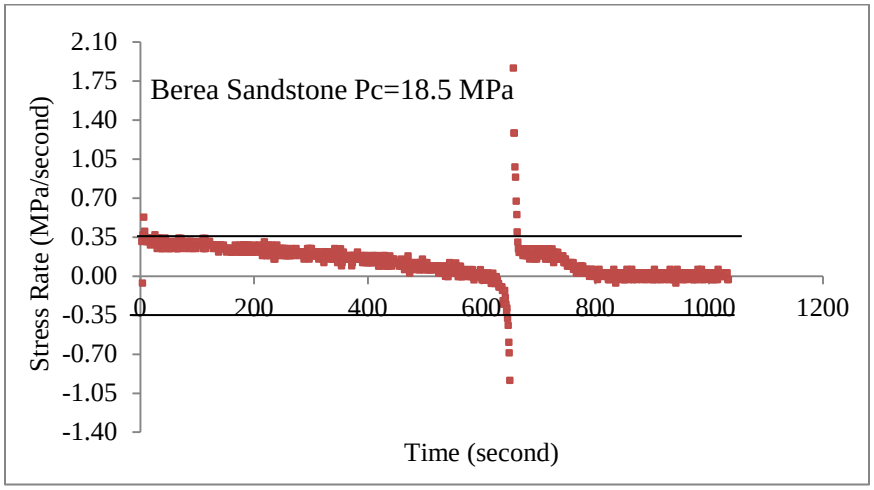

Fig. 4.16 Instantaneous stress rate during triaxial compression test

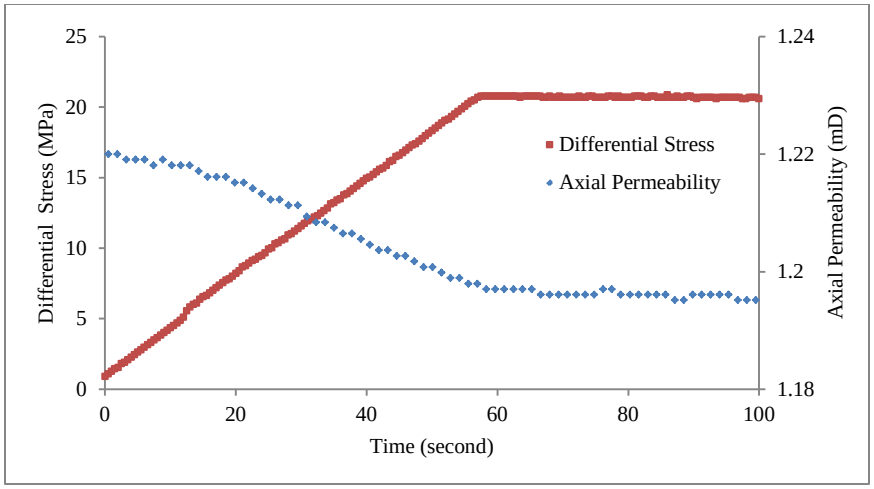

Fig. 4.17 Verification of axial permeability measurement with increasing stress

Therefore the stress rate used in the verification test was chosen to be 0.35 MPa/second. As Indiana limestone is less permeable than Berea sandstone, Indiana limestone specimen was chosen to perform the verification test. **Fig. 4.17** shows the result of verification test on Indiana limestone. It can be seen that the measured axial permeability is well correlated to stress change. This proves that continuous measurement of axial permeability on permeable Berea sandstone and Indiana limestone is feasible.

4.3.1 Berea sandstone

Continuous axial permeability measurement was performed during triaxial compression tests on Berea sandstone. **Figs. 4.18-21** show stress-strain curves and corresponding axial permeability variation of four triaxial compression tests at different confining pressures. In all tests, axial permeability keeps decreasing during rock deformation, even after rock breaks and macroscopic fracture forms.

Rock deformation is divided into three stages based on the characteristics of stress-strain curves. Three stages include linear elastic deformation, inelastic deformation, after fracturing (brittle behavior) or after peak strength (ductile behavior). In the stage of linear elastic deformation, the major deformation mechanisms include closure of pre-existing microcracks and grain compression. In the stage of inelastic deformation, microcracking develops in rock specimen. At low confining pressure, the stress-induced microcracks tend to coalesce and become localized, leading to brittle fracturing of rock specimen characterized by drastic drop in differential stress. While at high confining pressure, microcracking tends to develop homogeneously throughout rock specimen and results in more ductile behavior.

From Figs. 4.18-21, it is apparent that axial permeability variation is well correlated to different deformational stages. At low confining pressures (8.2 MPa, 18.5 MPa, Figs. 4.18-19), the closure of pre-existing microcraks and grain compression in the linear elastic deformation stage reduce pore space, which leads to axial permeability decrease. It is interesting to note that axial permeability decrease almost linearly at this stage. As rock specimen enters inelastic deformation, extensive microcracking tends to increase the overall pore space of rock specimen. This is evidenced by differential stress versus volumetric strain curves, where volumetric strain deflects from positive values (shrinkage of rock specimen) to negative values (dilatancy of rock specimen) before brittle fracturing. However, axial permeability does not increase due to the increase of porosity at this stage. Rather the decrease of axial permeability is accelerated. To understand this phenomenon, it is important to bear in mind that the intact Berea

sandstone is very permeable, with an initial fluid permeability of about 90 mD. Pore space is homogeneously distributed and well-sorted, and flow paths are well established. As rock specimen is deformed under stress, microcracking tends to destroy original pore structures and flow paths. As a result, the tortuosity of pore space is significantly increased, which leads to accelerated axial permeability decrease. At the time of brittle fracturing, the decrease of axial permeability is further accelerated (more obvious in Fig. 4.18). The creation of macroscopic fracture (Fig. 4.5) does not increase the ease of fluid flow in the axial direction. This can be explained when comparing intact rock surface and fracture rock surface of SEM images in later sections. As fractured rock specimen starts sliding, axial permeability continues to decrease at a lower speed.

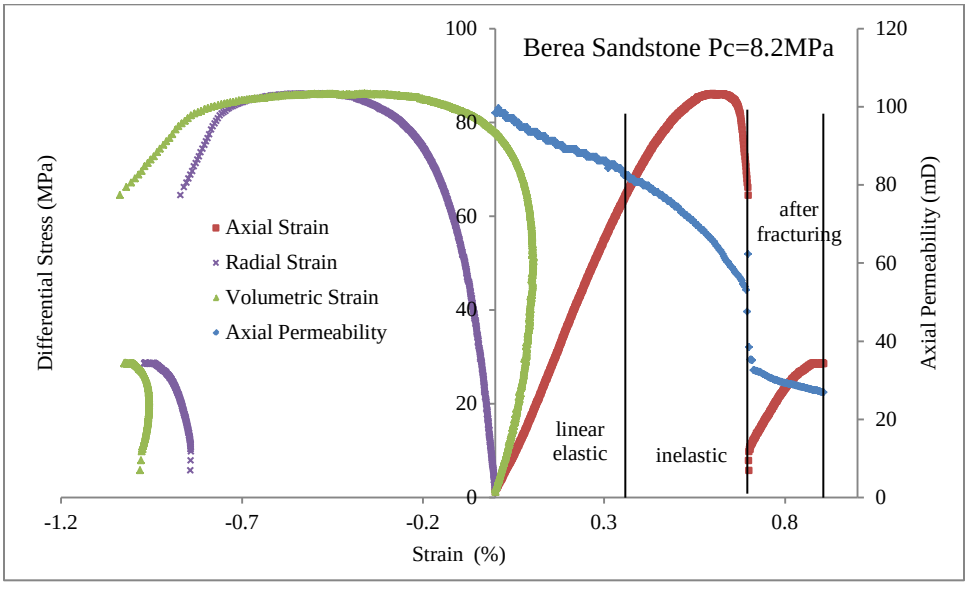

Fig. 4.18 Differential stress and axial permeability versus strain (Berea sandstone Pc = 8.2 MPa)

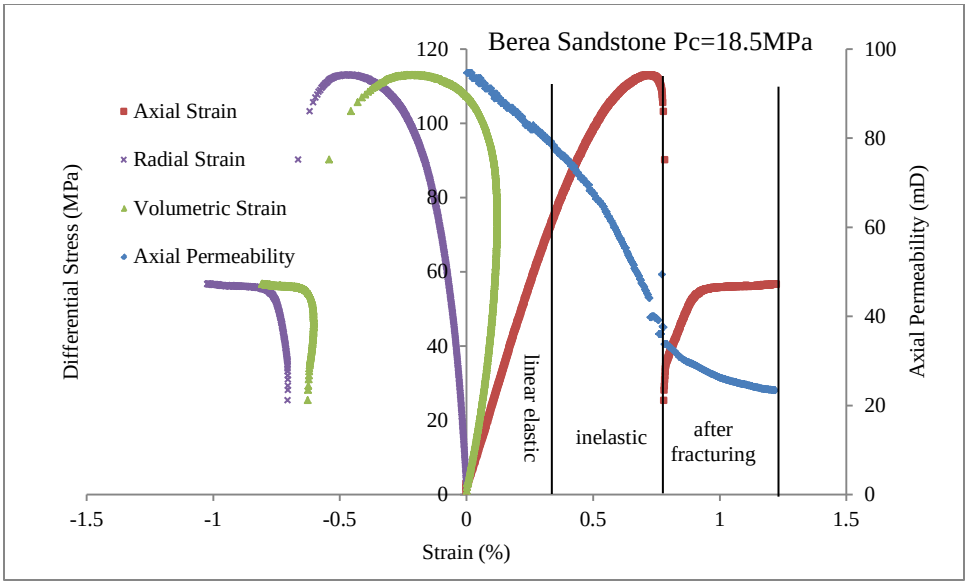

Fig. 4.19 Differential stress and axial permeability versus strain (Berea sandstone Pc = 18.5 MPa)

At higher confining pressures (32.2 MPa, 45.9 MPa, **Figs. 4.20-21**), axial permeability also decreases linearly at linear elastic deformation stage. In the inelastic deformation stage, dilatancy of rock specimen is more compressed. As shown in differential stress versus volumetric strain curve, the volumetric strain stays positive before peak strength and indicates overall shrinkage of rock specimen (therefore overall decrease of pore space). At this stage, the decrease of axial permeability is slightly accelerated. At around peak strength, axial permeability curve tends to level off. As rock specimen behaves more ductile, no drastic drop in axial permeability due to brittle fracturing is observed and variation of axial permeability tends to be much smoother. It seems that more distributed microracking at high confining pressure has similar impact

on axial permeability as at low confining pressure, except at the time of brittle fracturing.

Zhu and Wong (1997) observed similar phenomenon from triaxial compression tests on different sandstones. Before the onset of dilatancy, both axial permeability and porosity decrease with increasing stress. As rock starts dilating, axial permeability continues to decrease. And the formation of shear-induced fracture accelerates the decrease of axial permeability.

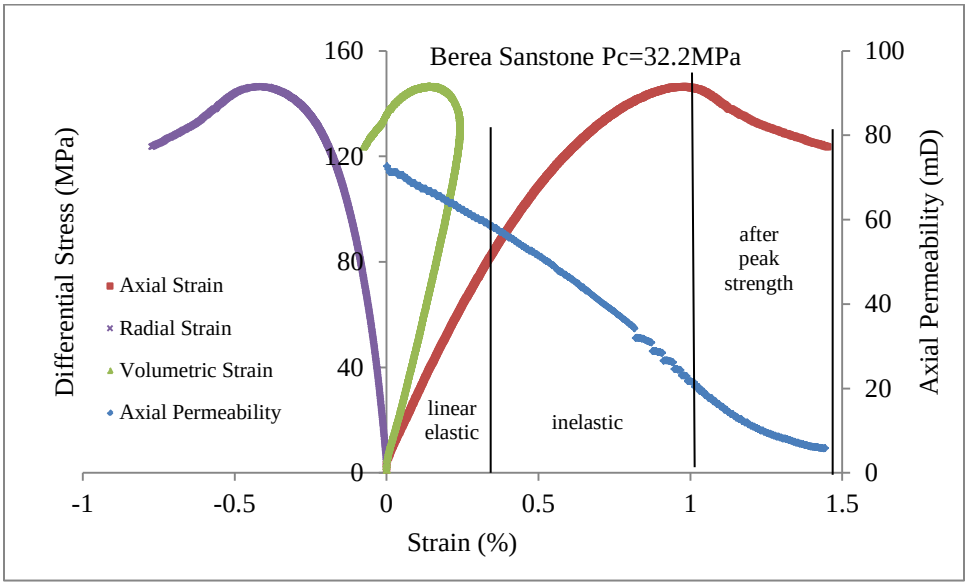

Fig. 4.20 Differential stress and axial permeability versus strain (Berea sandstone Pc = 32.2 MPa)

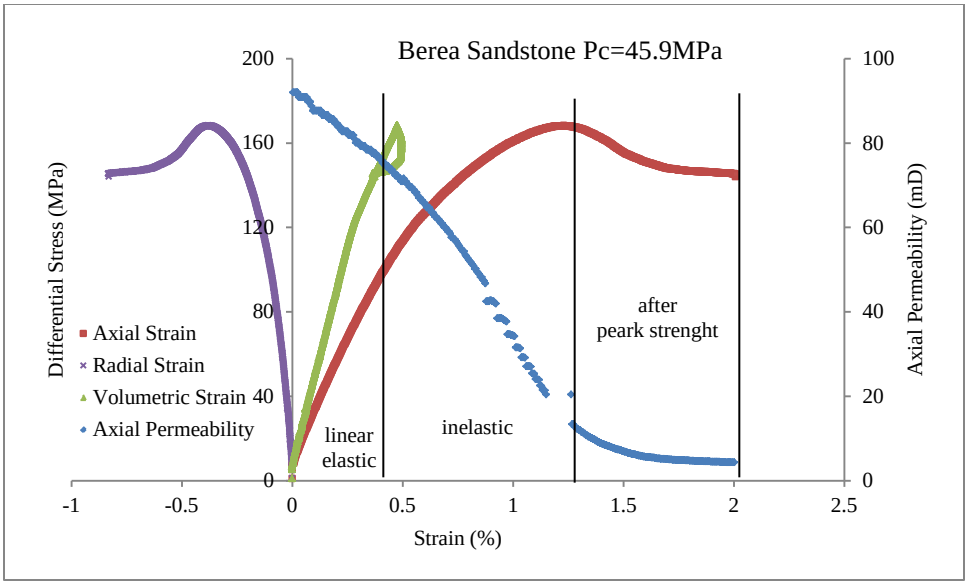

Fig. 4.21 Differential stress and axial permeability versus strain (Berea sandstone Pc = 45.9 MPa)

In order to better understand the impact of rock deformation on axial permeability change, SEM images were obtained for both intact and broken rock surfaces under same magnification **(Fig. 4.22)**. The left SEM image clearly shows grains of Berea sandstone. In the right SEM image, grain is no longer observable. Instead, almost all of the pore space is filled with fine particles. This helps explain the drastic reduction of axial permeability at the time of brittle fracturing.

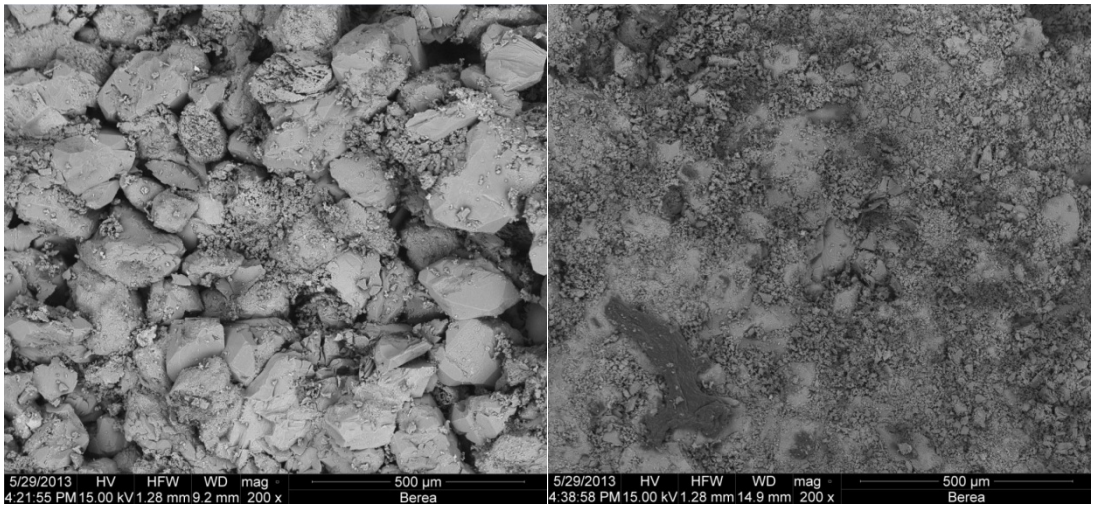

Fig. 4.22 SEM images of Berea sandstone: Left, intact rock surface; Right, fracture rock surface (200x magnification)

4.3.2 Indiana limestone

Continuous axial permeability measurement was also performed during triaxial compression tests on Indiana limestone. **Figs. 4.23-25** show stress-strain curves and corresponding axial permeability change of three triaxial compression tests at different confining pressures. The axial permeability of intact Indiana limestone is around 1 mD. Although Indiana limestone is much less permeable than Berea sandstone, the axial permeability variation of Indiana limestone is in general similar to that of Berea sandstone.

As with Berea sandstone, rock deformation is divided into three stages based on the characteristics of stress-strain curves: linear elastic deformation, inelastic deformation and after peak strength. It can be seen that Indiana limestone demonstrates appreciable ductile behavior. No drastic drop in differential stress is observed at low

confining pressure (10.9 MPa) and work hardening is observable at high confining pressure (17.4 MPa). Therefore it is believed that inelastic deformation such as microcracking is more homogeneously developed in the rock specimen.

For Indiana limestone, the variation of axial permeability is also well correlated to different deformational stages. At all three tested confining pressure levels, the variation of axial permeability behaves very similar in the first two stages. In the linear elastic deformation stage, axial permeability decreases at relatively lower speed. Unlike Berea sandstone, the decrease of axial permeability no longer resembles linear relationship. In the inelastic deformation stage, axial permeability tends to decrease more rapidly. It is interesting to note that the decrease of axial permeability first accelerates and then decelerates, which is shown in all three tests. This phenomenon can be also observed in the Berea sandstone which exhibits ductile behavior. At this stage, it seems that initial alteration of pore space by process like microcracking has a stronger impact on axial permeability. As pore space is further altered, the decrease of axial permeability tends to stabilize to a lower speed. In the third stage, different Indiana specimen behaves rather differently. At low confining pressure (10.9 MPa), axial permeability reverses from decrease to increase. At intermediate confining pressure (17.4 MPa), axial permeability increases slightly at the end. While at high confining pressure (30.2 MPa), axial permeability decreases slightly at the end.

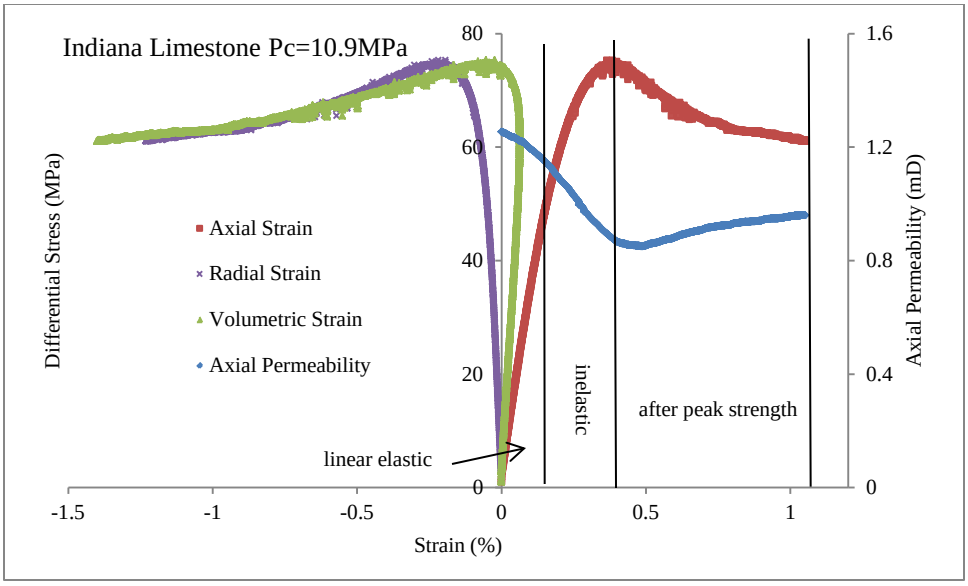

Fig. 4.23 Differential stress and axial permeability versus strain (Indiana limestone Pc = 10.9 MPa)

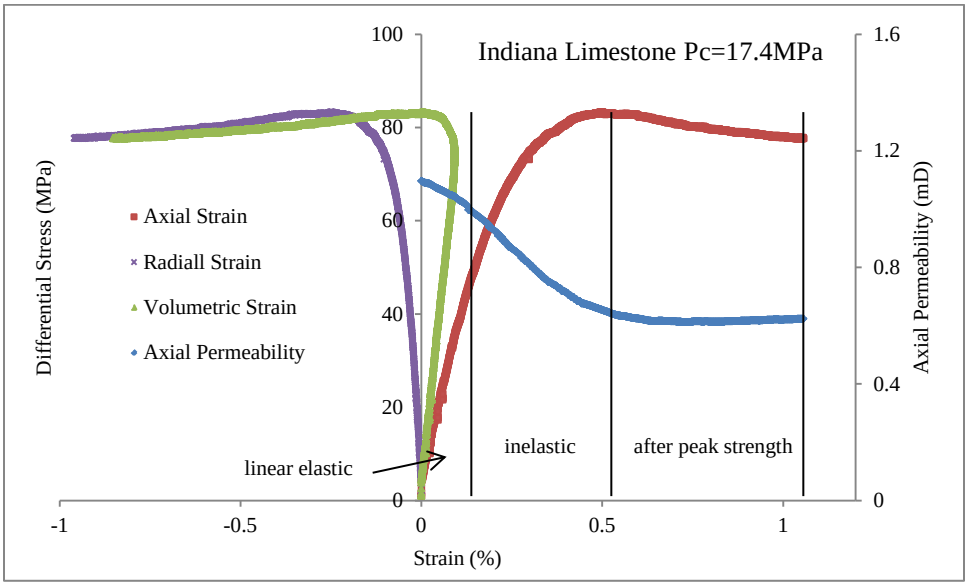

Fig. 4.24 Differential stress and axial permeability versus strain (Indiana limestone Pc = 17.4 MPa)

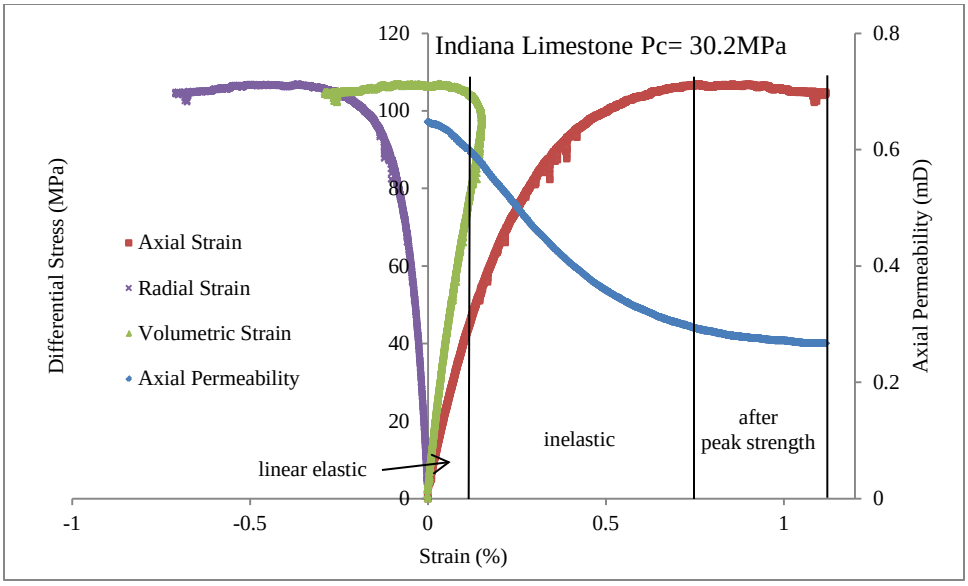

Fig. 4.25 Differential stress and axial permeability versus strain (Indiana limestone Pc = 30.2 MPa)

SEM pictures images were also obtained for both intact and broken rock surfaces of Indiana limestone. As can be seen in **Fig. 4.26**, the intact rock surface and the fracture rock surface are comparable. The left SEM image shows grains of Indiana limestone are well cemented and almost indistinguishable. Several microcracks are observable. In the right SEM image, fine particles produced by fracturing and sliding are also observable. Microcracks are also observable. However, pore structure was not altered as significantly as for Berea sandstone. It is possible that the formation of macroscopic fracture plays a different role on Indiana limestone. In Berea sandstone, the formation and sliding of macroscopic fracture produces abundance fine particles which are pushed into pore spaces, leading to dramatic decrease in axial permeability. However, Indiana limestone is much less permeably and not many fine particles are produced. Therefore,

pore space and microcracks are connected after formation of fracture, which results in an increase in axial permeability. From Fig. 4.9 we can see that the rock specimen tested at low confining pressure (10.9 MPa) developed a single fracture, while the other two specimens tested at higher confining pressures (17.4 MPa, 30.2 MPa) have no noticeable fractures. The presence of macroscopic fracture helps connect pore space and microcracks on two sides of fracture surface, which results in the increase of axial permeability after failure. While at confining pressure of 30.2 MPa, rock specimen exhibits work hardening, which indicates the shear-enhanced cataclastic flow as the major deformation mechanism. As microcracking distributes fairly homogenously throughout rock specimen, pore structure is further altered, resulting in increasing tortuosity and decreasing axial permeability. The test at confining pressure of 17.4 MPa seems to be transitional, microcracking distributes rather locally. The variation of axial permeability depends on the extent of localization of inelastic deformation.

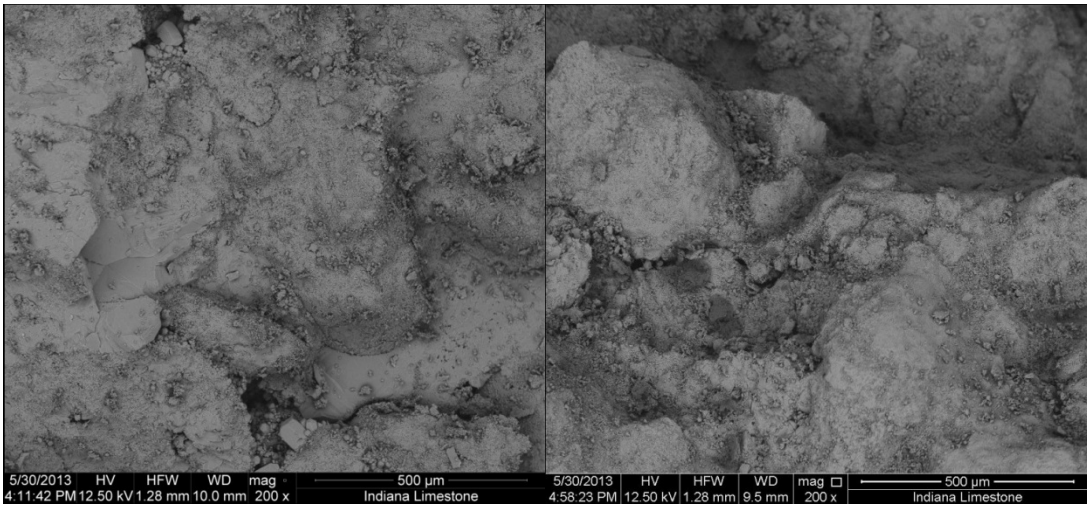

Fig. 4.26 SEM images of Indiana limestone: Left, intact rock surface; Right, fracture rock surface (200x magnification)

4.3.3 Westerly granite

The permeability of intact Westerly granite is in nanodarcy scale; our experimental setup is not capable of measuring such a low permeability. As a result, axial permeability was not measured for Westerly granite before failure. However, attempts were made to measure the axial permeability after rock failure. For uniaxial compression test, multiple vertical fractures were created after failure. Rock specimen was kept at a constant initial hydrostatic pressure of 10.4 MPa for some time, which allowed the fractured dry specimen to be fully saturated. The saturation process was long enough so that a steady flow of pore fluid was established. Then hydrostatic pressure was increased at a constant rate of 3.5 MPa/min, which was slow enough to allow continuous axial permeability measurement. **Fig. 4.27** shows the hydrostatic pressure and axial permeability versus volumetric strain. As shown in the plots, the decrease of axial permeability experiences two stages. At initial loading, axial permeability decreases rapidly, which is mostly due to the rapid initial fracture closure. As hydrostatic pressure further increases, the contact of fracture planes reaches a point that fracture closure slows down. As a result, the decrease of axial permeability slows down as well.

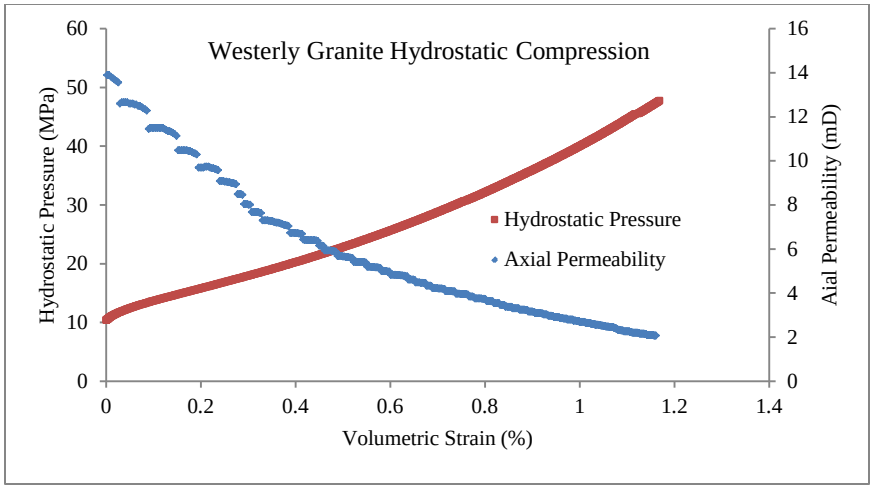

Fig. 4.27 Hydrostatic pressure and axial permeability versus volumetric strain (Uniaxially fractured Westerly granite)

For triaxial compression test at confining pressure of 6.9 MPa, it was also attempted to measure axial permeability after rock failure. However, the jacket that separates rock specimen from confining oil was broken during saturation. As a result, axial permeability measurement was not successful. For triaxial compression test at confining pressure of 20.7 MPa, rock specimen was successfully saturated after failure. But soon after the start of hydrostatic compression test, specimen jacket was broken again. During triaxial compression test, jacket was already deformed with the deformation of rock specimen. Therefore, further deformation of rock specimen can easily break jacket, which is a major problem for axial permeability measurement of fractured rock. However, the initial axial permeability of fractured rock specimen at confining pressure of 20.7 MPa was obtained from the saturation process. The determined axial permeability is 0.55 mD, which is much lower than that of uniaxially fractured specimen. As can be seen in Fig. 4.12, uniaxial compression created multiple

vertical fractures, while only one fracture connects the end surfaces of rock specimen for triaxial compression test at 20.7 MPa confining pressure. This is probably the main reason that uniaxially fractured specimen has a much higher initial axial permeability.

4.3.4 Summary

In this section, the axial permeability data was analyzed along with triaxial compression test data for Berea sandstone, Indiana limestone and Westerly granite. SEM images were used to improve the understanding of the effect of rock deformation on axial permeability variation. Axial permeability can be well correlated to different rock deformational stages. It was found that rock deformation alters pore structures and hence impact fluid flow through rock. For permeable rock like Berea sandstone and Indiana limestone, the destruction of pore structure by rock deformation usually leads to the decrease of axial permeability. For tight rock like Westerly granite, fractures created by rock deformation significantly improve the ease of fluid flow.

4.4 Acoustic emission monitoring

It was intended to monitor acoustic emission response during triaxial compression and axial permeability measurement. However, the flow of pore fluid generates significant amount of high strength noise, which completely blankets the signal generated during rock deformation. As a result, there is no point to monitor AE during triaxial compression with axial permeability measurement as no valuable information can be obtained. In order to obtain AE data of Berea sandstone and Indiana limestone, AE monitoring was performed on a different set of specimens without axial permeability measurement at corresponding confining pressures. This set of specimens

was prepared from the same block for axial permeability measurement. For Westerly granite and tuff, AE monitoring was conducted on the same set of specimens as axial permeability measurement was only attempted after rock failure.

4.4.1 Berea sandstone

AE monitoring was performed on Berea sandstone at confining pressures of 8.2 MPa, 18.5 MPa, 32.2 MPa and 45.9 MPa, which correspond to the confining pressure levels used in the axial permeability measurement. The threshold amplitudes used in these tests are around 55 dB. **Figs. 4.28-31** show stress-strain curves as well as AE rate versus axial strain curve. AE data was collected with the change of time. The axial strain in the AE rate curve was converted from time by multiplying strain rate applied during triaxial compression test.

At confining pressure of 8.2 MPa (Fig. 4.28), AE rate stays at low level at the early stage of loading. It increases with increasing stress. After peak strength, AE rate reaches its peak value and maintains at high level until the final fracturing of rock specimen.

At confining pressure of 18.5 MPa (Fig. 4.29), AE rate keeps increasing until the time of rock failure. It drops to a low level with the drop of differential stress at the time of brittle fracturing. As broken rock specimen starts sliding, AE rate climbs and maintains at a level during steady frictional sliding.

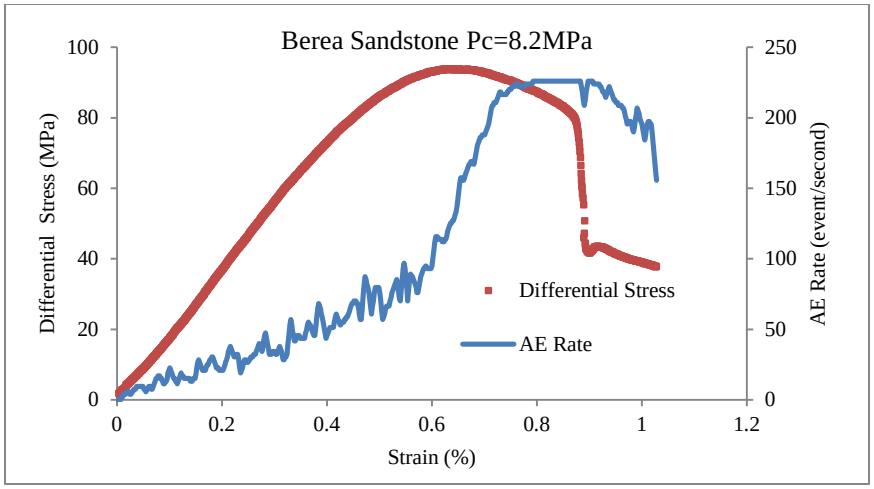

Fig. 4.28 Differential stress and AE rate versus axial strain (Berea sandstone Pc = 8.2 MPa)

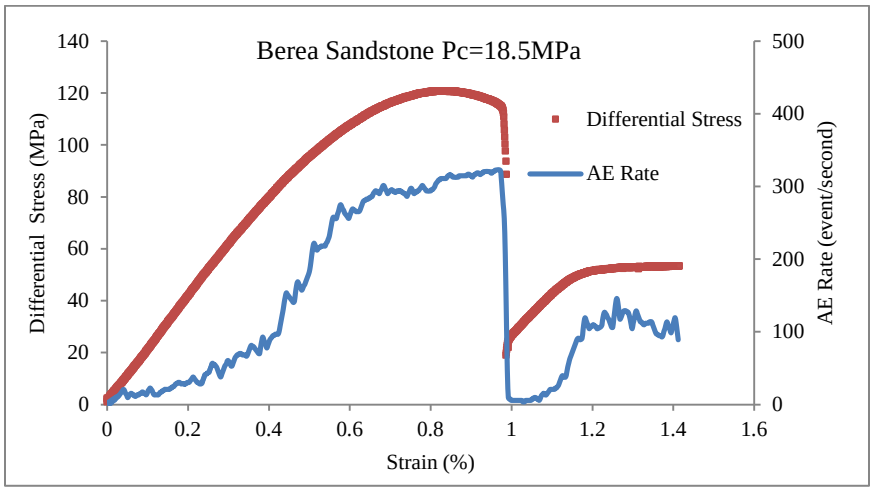

Fig. 4.29 Differential stress and AE rate versus axial strain (Berea sandstone Pc = 18.5 MPa)

At higher confining pressure levels (32.2 MPa and 45.9 MPa, **Figs. 4.30-31**), AE rate quickly increases to its peak value and maintains at this high level until sliding occurs. It is interesting to note that the highest AE rate at confining pressures of 18.5 MPa, 32.2 MPa and 45.9 MPa is consistently similar, which is around 300 events/second. High AE rate marks strong microcracking during loading. It is apparent that higher confining pressure leads to longer period of strong microcracking. As a result, pore structure would be more severely destroyed, resulting in more pronounced permeability decrease.

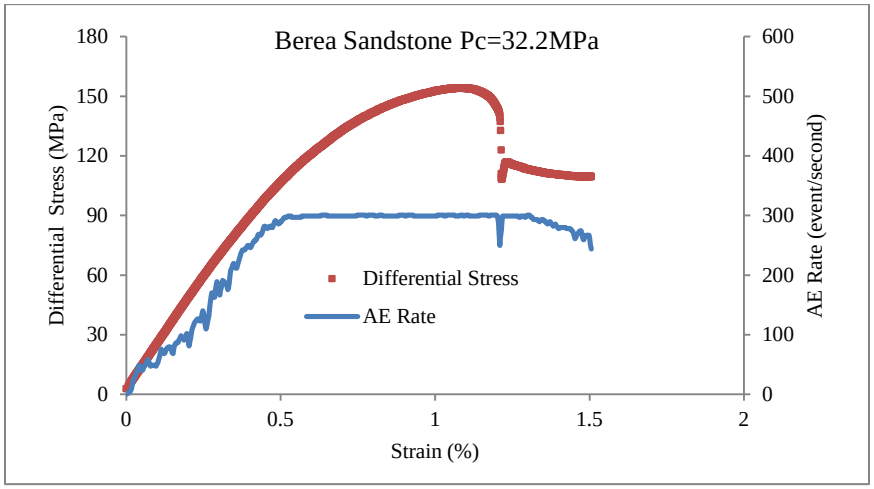

Fig. 4.30 Differential stress and AE rate versus axial strain (Berea sandstone Pc = 32.2 MPa)

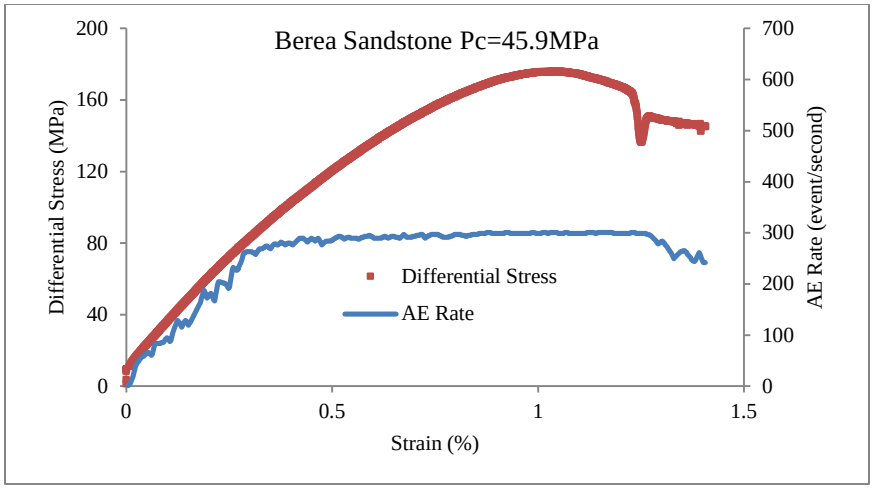

Fig. 4.31 Differential stress and AE rate versus axial strain (Berea sandstone Pc = 45.9 MPa)

4.4.2 Indiana limestone

AE monitoring was performed on Indiana limestone at confining pressures of 10.9 MPa, 17.4 MPa and 30.2 MPa, which correspond to the confining pressure levels used in the axial permeability measurement. The threshold amplitudes used in these tests are around 45 dB. **Figs. 4.32-34** show stress-strain curves as well as AE rate versus axial strain curve.

Even though the threshold amplitude of Indiana limestone is lower than that of Berea sandstone, AE signal for Indiana limestone is almost negligible. The highest AE rate in three tests is only 3 events/second, while for Berea sandstone the highest AE rate is over 300 events/second. This indicates different deformation mechanisms for Berea sandstone and Indiana limestone. Micromechanical study by Menéndez et al. (1996) shows that inelastic deformation of clastic rock, such as Berea sandstone, primarily results from grain crushing initiated by the stress concentration at grain contacts. While

for limestone, the inelastic deformation mainly comes from pore collapse, which initiates from stress concentration on the surface of pore structure. It seems that grain crushing in Berea sandstone produces much higher acoustic energy, comparing to pore collapse in Indiana limestone.

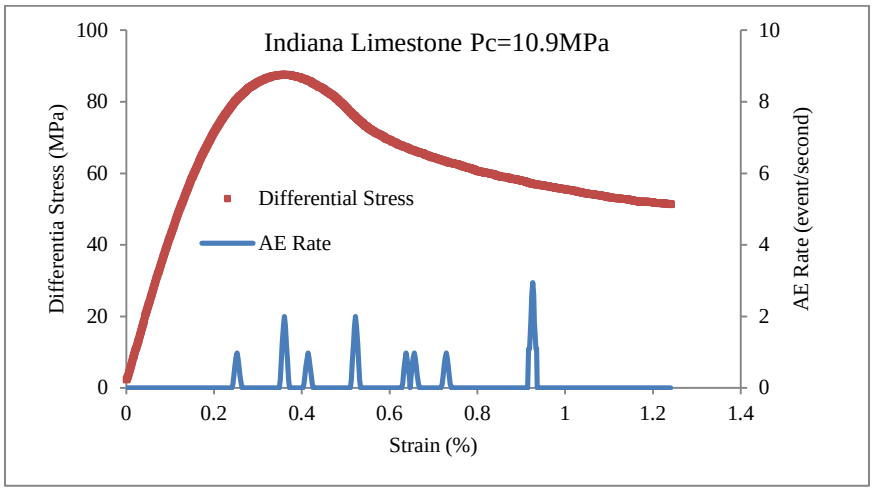

Fig. 4.32 Differential stress and AE rate versus axial strain (Indiana limestone Pc = 10.9 MPa)

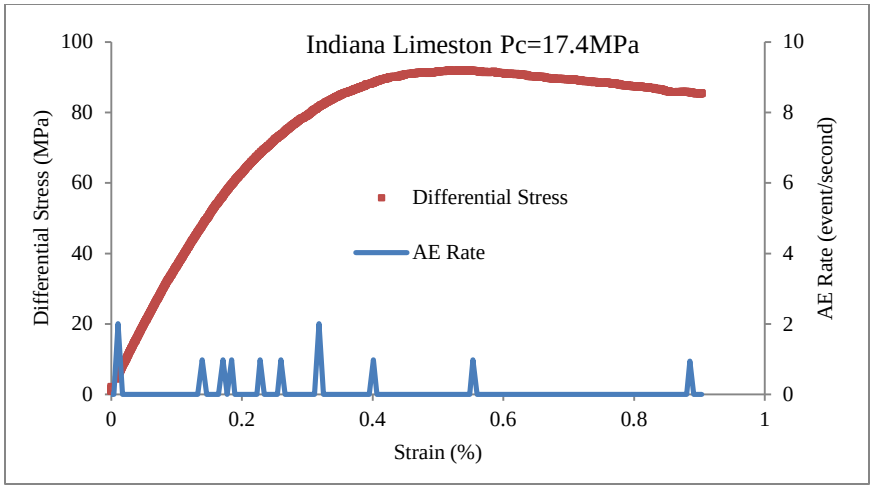

Fig. 4.33 Differential stress and AE rate versus axial strain (Indiana limestone Pc = 17.4 MPa)

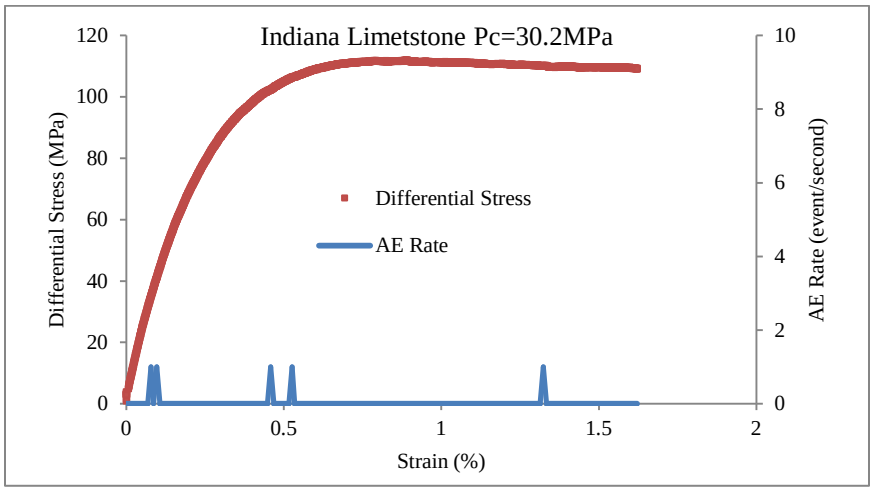

Fig. 4.34 Differential stress and AE rate versus axial strain (Indiana limestone Pc = 30.2 MPa)

4.4.3 Westerly granite

AE monitoring was conducted for all three compression tests on Westerly granite. **Figs. 4.35-37** show stress-strain curves as well as AE rate versus axial strain curve.

For uniaxial compression test, AE rate increases with increasing axial strain and reaches its peak value at the time of failure. After failure, AE rate decreases to almost zero. It can be seen in Fig. 4.12 that several vertical fractures were created. As axial strain further increases, rock specimen almost lost its entire load carrying capability.

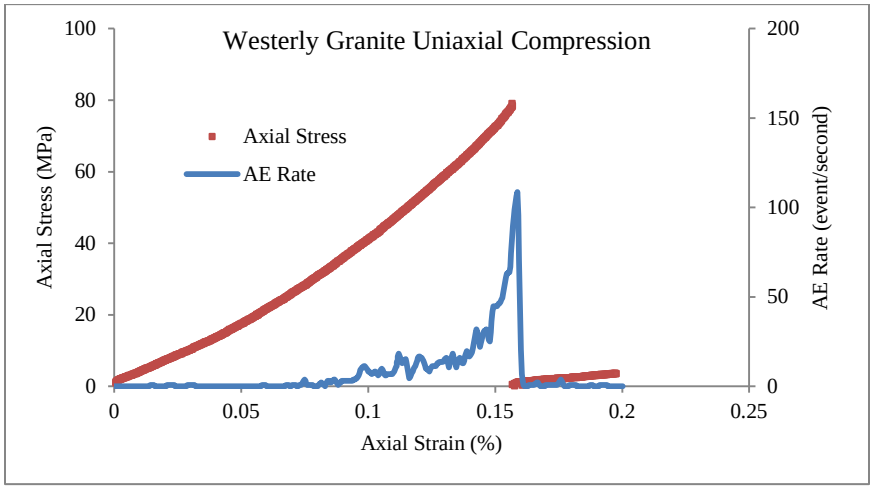

Fig. 4.35 Differential stress and AE rate versus axial strain (Westerly granite uniaxial compression)

For triaxial compression at confining pressure of 6.9 MPa (Fig. 4.36), AE rate increases with increasing axial strain and reaches its peak value before failure. At the time of failure, AE rate drops and then immediately goes back to peak value as fractured

rock specimen slides. It can be seen that rock sliding generates relatively constant AE response.

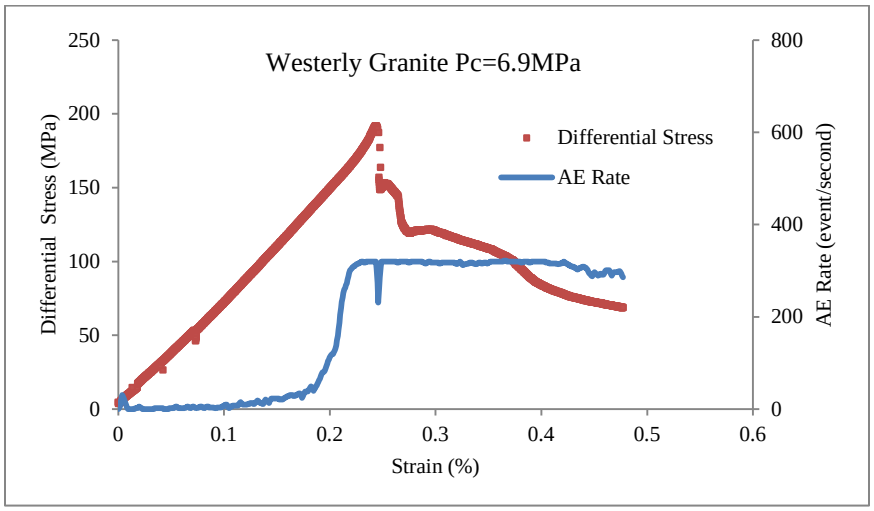

Fig. 4.36 Differential stress and AE rate versus axial strain (Westerly granite Pc = 6.9 MPa)

For triaxial compression test at confining pressure of 20.7 MPa (Fig. 4.37), similarly, AE rate increases with increasing axial strain and reaches its peak value before failure. Comparing to lower confining pressure, the peak value of AE rate is reached earlier with respect to the peak strength of rock specimen. At the time of failure, AE rate doesn't drop but maintains at the peak value.

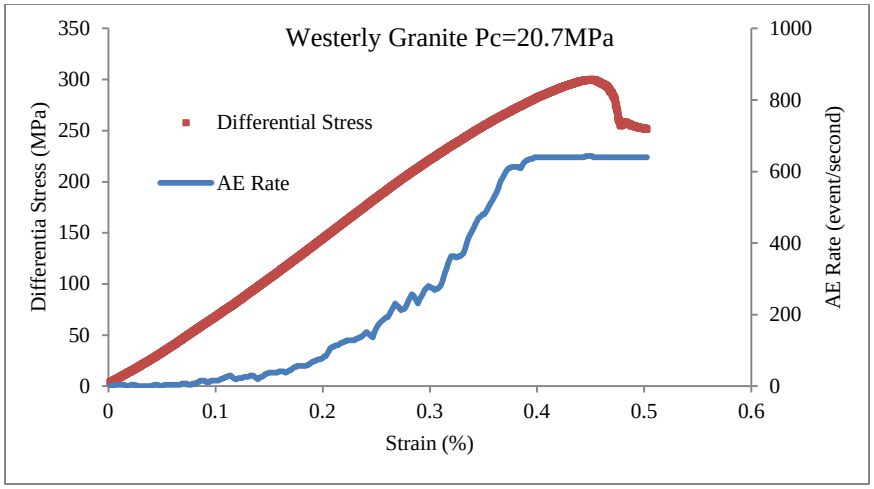

Fig. 4.37 Differential stress and AE rate versus axial strain (Westerly granite Pc = 20.7 MPa)

For three different compression tests, peak AE rate increases with increasing confining pressure. This indicates that more damage is accumulated in rock to arrive at failure at higher confined conditions.

4.4.4 Tuff

AE monitoring was performed on all three tuff specimens at the same confining pressure. The AE response of tuff specimens is different from all other three rock types (**Figs. 4.38-40**). In the linear elastic part of the stress-strain curve, AE rate is almost zero. As rock starts yielding, AE rate increases rapidly and attains its peak value after peak strength of rock. Unlike Berea sandstone and Westerly granite which almost maintain a constant peak value, AE rate fluctuates considerably at high level for tuff specimens. Comparing to Berea sandstone and Westerly granite, the peak value of AE rate for tuff is much lower, which is below 50 events/second.

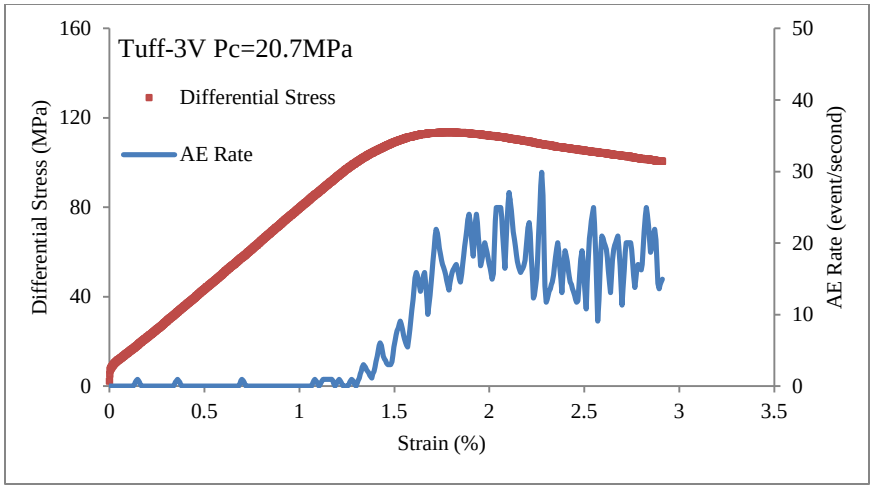

Fig. 4.38 Differential stress and AE rate versus axial strain (Tuff-3V Pc = 20.7 MPa)

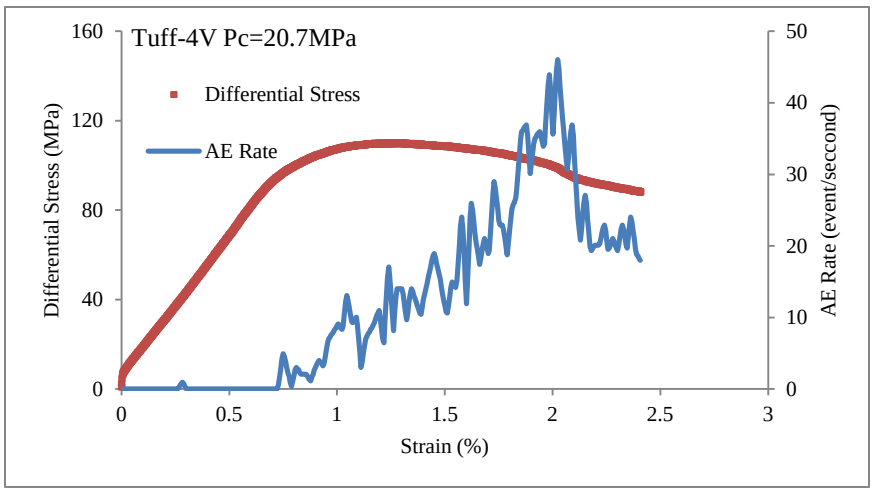

Fig. 4.39 Differential stress and AE rate versus axial strain (Tuff-4V Pc = 20.7 MPa)

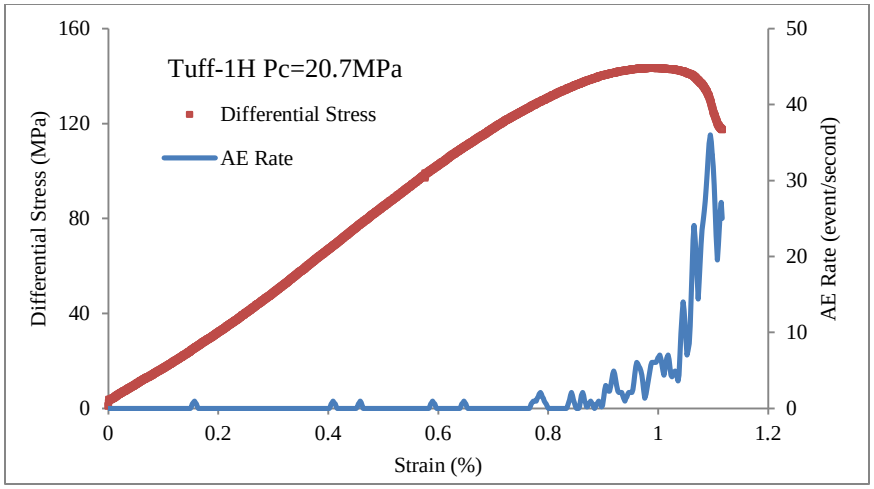

Fig. 4.40 Differential stress and AE rate versus axial strain (Tuff-1H Pc = 20.7 MPa)

4.4.5 Summary

In this section, the AE data was analyzed along with triaxial compression test data of four types of rocks. Although each rock type has its unique AE response during rock deformation, it seems that the AE response can be well correlated to the brittleness and ductility of rock. Ductile rocks like Indiana limestone and tuff generate very low AE response, while brittle Berea sandstone and Westerly granite produce much higher AE rate throughout rock deformation.

5. CONCLUSION & RECOMMENDATION

In this study, four different rock types, including Berea sandstone, Indiana limestone, Westerly granite and tuff, were tested for mechanical, axial permeability and acoustic emission data. Based on experimental results, following conclusions can be drawn

1. Mechanical data shows that Berea sandstone and Westerly granite are relatively brittle, while Indiana limestone and tuff are relatively ductile.
2. Rock deformation alters pore structures and hence impact fluid flow through rock. For permeable rock like Berea sandstone and Indiana limestone, the destruction of pore structure by rock deformation usually leads to decrease of axial permeability. For tight rock like Westerly granite, fractures created by rock deformation significantly improve the ease of fluid flow.
3. AE response of rock deformation is strongly dependent on rock type. Brittle Berea sandstone and Westerly granite produce high AE rate during compression test, while ductile Indiana limestone and tuff generate very low AE rate.

Recommendations for future work are listed as follows

1. It is recommended to apply alternative permeability measurement technique to measure permeability variation of tight rock during triaxial compression test before failure.

2. It is also interesting to test more rock types with wider permeability range, so that more comprehensive study can be performed on the dependence of permeability on rock deformation.

REFERENCES

Böker, R. (1915). Die Mechanik der bleibenden Formänderung in kristallinisch aufgebauten Körpern (The mechanics of permanent deformation in chrystalline bodies). *Ver. dt. Ing. Mitt. Forsch., 175*, 1-51.

Brace, W. (1978). A note on permeability changes in geologic material due to stress. *Pure and Applied Geophysics, 116*(4-5), 627-633.

Brace, W., & Martin, R. (1968). A test of the law of effective stress for crystalline rocks of low porosity. *International Journal of Rock Mechanics and Mining Sciences & Geomechanics Abstracts, 5*(5), 415-426.

Brace, W., Walsh, J., & Frangos, W. (1968). Permeability of granite under high pressure. *Journal of Geophysical Research, 73*(6), 2225-2236.

Costin, L. (1983). A microcrack model for the deformation and failure of brittle rock. *Journal of Geophysical Research: Solid Earth (1978–2012), 88*(B11), 9485-9492.

Fortin, J., Stanchits, S., Dresen, G., & Gueguen, Y. (2009). Acoustic emissions monitoring during inelastic deformation of porous sandstone: comparison of three modes of deformation. *Pure and Applied Geophysics, 166*(5-7), 823-841.

Handin, J., & Hager Jr, R. V. (1957). Experimental deformation of sedimentary rocks under confining pressure: Tests at room temperature on dry samples. *AAPG Bulletin, 41*(1), 1-50.

Hirata, T. (1987). Omori's power law aftershock sequences of microfracturing in rock fracture experiment. *Journal of Geophysical Research: Solid Earth (1978–2012), 92*(B7), 6215-6221.

Holcomb, D. J. (1993). General theory of the Kaiser effect. *International Journal of Rock Mechanics and Mining Sciences & Geomechanics Abstracts, 30*(7), 929-935.

Kaiser, J. (1950). An investigation into the occurrence of noises in tensile tests, or a study of acoustic phenomena in tensile tests. *Ph. D. thesis, Tech. Hochsch. Munchen, Munich, Germany*.

Kranz, R., Satoh, T., Nishizawa, O., Kusunose, K., Takahashi, M., Masuda, K., & Hirata, A. (1990). Laboratory study of fluid pressure diffusion in rock using acoustic emissions. *Journal of Geophysical Research: Solid Earth (1978–2012), 95*(B13), 21593-21607.

Lei, X. L., Kusunose, K., Nishizawa, O., Cho, A., & Satoh, T. (2000). On the spatio‐temporal distribution of acoustic emissions in two granitic rocks under triaxial compression: The role of pre-existing cracks. *Geophysical Research Letters, 27*(13), 1997-2000.

Lockner, D. (1993). The role of acoustic emission in the study of rock fracture. *International Journal of Rock Mechanics and Mining Sciences & Geomechanics Abstracts, 30*(7), 883-899.

Lockner, D., & Byerlee, J. (1977). Acoustic emission and creep in rock at high confining pressure and differential stress. *Bulletin of the Seismological Society of America, 67*(2), 247-258.

Menéndez, B., Zhu, W., & Wong, T. f. (1996). Micromechanics of brittle faulting and cataclastic flow in Berea sandstone. *Journal of Structural Geology, 18*(1), 1-16.

Paterson, M. (1958). Experimental deformation and faulting in Wombeyan marble. *Geological Society of America Bulletin, 69*(4), 465-476.

Scholz, C. (1968). Microfracturing and the inelastic deformation of rock in compression. *Journal of Geophysical Research, 73*(4), 1417-1432.

Stanchits, S., Vinciguerra, S., & Dresen, G. (2006). Ultrasonic velocities, acoustic emission characteristics and crack damage of basalt and granite. *Pure and Applied Geophysics, 163*(5-6), 975-994.

Terzaghi, K. (1923). Die Berechnung der Durchlässigkeitsziffer des Tones aus dem Verlauf der hydrodynamischen Spannungserscheinungen. *Akad Wissensch Wien Sitzungsber Mathnaturwissensch Klasse IIa, 132*, 105-124.

von Kármán, T. (1911). Festigkeitsversuche unter allseitigem Druck (Strength measurements under uniforme pressure). *Zeit. Ver. dt. Ing., 55*, 1749-1757.

Walsh, J. (1981). Effect of pore pressure and confining pressure on fracture permeability. *International Journal of Rock Mechanics and Mining Sciences & Geomechanics Abstracts, 18*(5), 429-435.

Wang, J. A., & Park, H. (2002). Fluid permeability of sedimentary rocks in a complete stress-strain process. *Engineering Geology, 63*(3), 291-300.

Wong, T. f., David, C., & Zhu, W. (1997). The transition from brittle faulting to cataclastic flow in porous sandstones: Mechanical deformation. *Journal of Geophysical Research: Solid Earth (1978–2012), 102*(B2), 3009-3025.

Zhu, W., & Wong, T. f. (1997). The transition from brittle faulting to cataclastic flow: Permeability evolution. *Journal of Geophysical Research: Solid Earth (1978–2012), 102*(B2), 3027-3041.

Zoback, M. D., & Byerlee, J. D. (1975). Permeability and effective stress: Geologic note. *AAPG Bulletin, 59*(1), 154-158.

Zoback, M. D., & Byerlee, J. D. (1976). Effect of high-pressure deformation on permeability of Ottawa sand. *AAPG Bulletin, 60*(9), 1531-1542.